Precambrian Research 435 (2026) 108038

Contents lists available at ScienceDirect

Precambrian Research

journal homepage: www.elsevier.com/locate/precamres

A ~1.6 Ga accretionary event in the polymetamorphic Lesser Himalaya, India: Insights into late-stage assembly of the Columbia supercontinent

Mallickarjun Joshi [a], Biraja P. Das [a,b,c,*], Shubham Patel [a], Daniel Pastor-Galán [d,e], Naresh C. Pant [b], A. Krishnakanta Singh [f], Govind Oinam [g], Alok Kumar [a], Ankit Kumar [a]

[a] Centre of Advanced Study in Geology, Institute of Science, Banaras Hindu University, Varanasi 221005, India
[b] Department of Geology, University of Delhi, New Delhi 110007, India
[c] Department of Geology, Dharanidhar University, Keonjhar 758001, India
[d] Instituto de Geociencias (IGEO), CSIC, Spain
[e] Frontier Research Institute for Interdisciplinary Science, Tohoku University, Sendai, Japan
[f] Department of Applied Geology, Dr. HarisinghGour University, Sagar 470003, Madhya Pradesh, India
[g] Wadia Institute of Himalayan Geology, Dehradun 248001, India

ARTICLE INFO

Keywords:
Himalaya
Askot Klippe
Almora Nappe
High-Resolution Garnet *P-T* path
Isochemical phase diagram
Thermobarometry

ABSTRACT

A series of collisions among most of the continental fragments between 2.1 Ga and 1.8 Ga culminated in the assembly of the Columbia supercontinent. Vestiges of reworked Northern Indian Continental Margin, involved in the Columbia supercontinent assembly, are preserved and known as the 'Paleoproterozoic high-grade metapelitic gneisses in the Askot Klippe' of NW Lesser Himalaya. We report new whole-rock geochemistry, inverse and forward geothermobarometric modeling, isochemical phase diagram modeling, and U–Pb zircon dating of metapelitic schists and gneisses to decode the multiple metamorphic histories in Lesser Himalayan fold-thrust. We identify two metamorphic events that mark the Columbia Supercontinent assembly's accretion phases: an earlier ca. 1.85 Ga age related to the first metamorphic episode and a second age of ca. 1.62 Ga associated with the youngest reported collisional event related to subduction followed by accretion of crust and attendant crustal anatexis. The earlier event reached upper green-schist facies metamorphism during which garnet cores crystallized, whereas the second event indicates amphibolite-granulite peak metamorphic conditions. Our results show that the amalgamation of Columbia persisted until at least ca. 1.62 Ga in the northwestern Lesser Himalaya, indicating tectonic continuity between the northern Indian continental margin, the Aravalli–Delhi Mobile Belt, and the Eastern Cathaysia Block—key elements in the final Paleoproterozoic assembly of the Columbia supercontinent.

1. Introduction

The concept that Earth's continents cyclically assemble into larger-scale continents termed supercontinents is increasingly accepted in the Earth Sciences community. Yet, Pangea is the only supercontinent for which accurate reconstructions exist, with first-order constraints on its configuration (e.g., Mitchell et al., 2012; Ernst et al., 2013; Nance and Murphy, 2013; Stampfli et al., 2013; Pastor-Galan, 2022). Supercontinents are generally conceived as rigid super-plates, characterized by minimal internal tectonic activity, limited interaction between the lithosphere and the underlying mantle (e.g., Rogers and Santosh, 2009; Pastor-Galan et al., 2019). Cycles of supercontinent assembly and breakup have been tentatively linked to major geological processes, including sea-level fluctuations, changes in biogeochemical cycles, shifts in global climate, variations in continental margin sedimentation, the creation of large igneous provinces, deep mantle convection, outer core dynamics, and alterations in Earth's magnetic field (Worsley et al., 1985; Nance and Murphy, 1994; Nance, 2022; Martin et al., 2024).

One of the most debated ancient supercontinents is Columbia, also known as Nuna (see Hou et al., 2008; Zhang et al., 2012; Meert, 2014 for a discussion on supercontinent "branding"), initially proposed based on the widespread occurrences of 2.1–1.8 Ga orogenic belts (e.g., Rogers and Santosh, 2002; Zhao et al., 2004; Meert and Santosh, 2017; Xia and Xu, 2019). The assembly attained the maximum weldment at ~1.8 Ga

* Corresponding author.
E-mail address: birajageology@gmail.com (B.P. Das).

https://doi.org/10.1016/j.precamres.2026.108038
Received 20 August 2025; Received in revised form 28 January 2026; Accepted 31 January 2026
Available online 6 February 2026

followed by protracted subduction-related outgrowth through several accretionary orogens along the margins of the continents at ~1.8–1.5 Ga (Zhao et al., 2004). After a prolonged subduction-accretion process, Columbia started to rift along its margin at ~1.6–1.4 Ga (Rogers and Santosh, 2002; Zhao et al., 2004). Most reconstructions suggest that Columbia incorporated nearly all of the existing Earth's continental blocks (Wilson, 1963; Nance et al., 1988; Rogers, 2000; Rogers and Santosh, 2002; Zhao et al., 2002; Hou et al., 2008). Zhao et al., (2002) identified widespread 'anorogenic magmatism' between 1.4 and 1.2 Ga, which they interpreted as the onset of Columbia's breakup. According to Rogers and Santosh (2002), Columbia supercontinent incorporated nearly all earth's continental cratonic fragments between 1.9 Ga and 1.5 Ga, having the Indian Continental Block (ICB) positioned close to East Antarctica to the south and North America (Laurentia) to the east, forming a cohesive unit. Zhao et al., (2004) configured the Columbia supercontinent by placing the ICB between the East Antarctica Craton to the south and the North China Craton to the north with ~1.8 Ga Central Indian Tectonic Zone (CITZ) as an extension of the ~1.85 Ga Trans-North China Orogen, facilitating the linkage of these blocks during Columbia's assembly. Hou et al. (2008) proposed a configuration model highlighting ~1.85 Ga giant radiating mafic dyke swarm that unites the North China Craton, Indian Craton, and Laurentia (Canadian Shield), with a stable core including Laurentia, West Australia, and East Antarctica. This clearly contradicts with earlier models like Zhao et al., (2002, 2004), which resemble Rodinia configurations. Johansson (2009) challenged the incorporation of the ICB in Columbia, renamed the supercontinent as "Midgardia" which focuses on a core assemblage of cratons without involvement of the position of ICB. Yu et al., (2012) modified the framework of Zhao et al., (2004) by incorporating the Cathaysia Block (part of South China) directly north of the ICB, with the Lesser Himalaya in northwest India connected to the South Korean Peninsula (SKP). Pisarevsky et al., (2013) proposed a paleogeographic reconstruction of Columbia, juxtaposing the ICB against the southern part of Baltica to form a single proto-craton, showing stable continental configurations by around 1.65–1.58 Ga. Grenholm et al., (2019) depicted that the Columbia assembly configuration started with the coalescence of the Atlantic Continental Block with the Fennoscandian continental blocks and the Siberian Craton at ca. 1.9–1.8 Ga. More recent evidence indicates that Columbia may not have fully formed until around 1.6 Ga (Kirscher et al., 2021; Volante et al., 2022); prolonging its originally proposed lifespan by ~200 Ma.

Columbia's exact configuration and duration still remain uncertain because of the uncertainties in dating key geological events. Although, paleomagnetic data remain as primary data limitations, geological indicators, including orogenic belts having Proterozoic rock records provide insufficient clues subjected to interpretive debates and biases. These features suggest global-scale collisions, but their interconnectedness in a single supercontinent model remains contested. Erosion, subduction, and metamorphism have destroyed much of the ancient record, further hindering definitive mappings. Meert (2014) even proposed that the similarities between reconstructions of Columbia and Rodinia may reflect cognitive biases or imply that plate tectonics processes operated differently in the deep past. After two decades of research, significant gaps remain regarding Columbia's configuration, which highlights the critical need for further geochronologic, and geological data from across all Columbia fragments.

The Northern Indian Continental Margin (NICM) represents the northernmost extent of the Paleoproterozoic Indian Shield (Hinsbergen et al., 2012) and contains widespread evidence of Proterozoic granitoids, mafic volcanics, and volcanic arc-related magmatic rocks (Sharma and Rashid, 2001; Miller et al., 2000; Richards et al., 2005; Kohn et al., 2010; Mandal et al., 2016; Phukon et al., 2018; Sen et al., 2019; Mukherjee et al., 2019; Mukherjee et al., 2024; Pandey, 2022; Patel et al., 2025). Parts of the NICM thrust southwards during the orogeny presently occur as metamorphic nappes and klippen in the Lesser Himalaya preserve evidence of pre-Himalayan metamorphism, with metamorphic grades ranging from low-grade greenschist facies to upper amphibolite-granulite transition facies in Lesser Himalayan nappes (Joshi and Singh, 1990; Joshi et al., 1994; Bhargava and Bassi, 1994; Pant et al., 2006; Joshi and Tiwari, 2004; 2007; 2009; Joshi et al., 2019; Das et al., 2019; Das et al., 2021; Mukherjee et al., 2024; Joshi et al., 2025). However, metamorphic and geochronological constraints remain sparse for the northernmost sectors of the Indian Shield, except for the age of 1891 ± 12.82 Ma, for the metapelitic gneisses of Baijnath Klippe, NW Lesser Himalaya (Joshi et al., 2025), limiting our ability to robustly link the Northwestern Lesser Himalaya with Columbia (see Hifzurrahman et al., 2021; Mukherjee et al., 2024; Joshi et al., 2025) and their relation with the surrounding continental blocks (cf. Rogers and Santosh, 2002; Zhao et al., 2002; 2004; Teixeira et al., 2007; Hou et al., 2008; Johansson, 2009; Pisarevsky et al., 2013; Reis et al., 2013; Wang et al., 2016; Grenholm et al., 2019; Terentiev and Santosh, 2020).

In this broader context, the Lesser Himalaya, forming a major component of the NICM, represents a critical but underexplored archive for evaluating the role of ICB in Columbia's assembly. Being triggered by the young Tertiary collision, Lesser Himalayan nappes and klippen hold the key to preserve the pre-Himalayan tectono-metamorphic signatures because of its magmatic and *meta*-volcanic rock association with the Paleoproterozoic NICM of Indian Craton (Kohn et al., 2010; Mukherjee et al., 2019; Yang et al., 2021; Patel et al., 2025). Furthermore, Lesser Himalaya marks an integral component of Indian Shield which may have received sediment supply from the Proterozoic Aravalli-Bundelkhand Craton and subsequently deformed and metamorphosed (Kaur et al., 2013).

The pre-Himalayan polymetamorphic histories of Lesser and High Himalayan sequences span from the Paleoproterozoic to the Paleozoic era (Joshi and Singh, 1990; Arita et al., 1990; Sorkhabi and Stump, 1993; Joshi et al., 1994; Paudel and Arita, 2000; Joshi and Tiwari, 2007, 2009; Lihter et al., 2022). However, robust chronological constraints for successive metamorphic events, particularly those of Paleoproterozoic age, remain limited. During the 2.1–1.8 Ga global-scale orogeny, the Indian Shield was an integral part of the Columbia supercontinent (Meert, 2012; Wang et al., 2023). Paleoproterozoic magmatic rocks present in the Himalayan fold-thrust belt demonstrate connections with the Aravalli-Delhi Mobile Belt and the Columbia supercontinent (Kaur et al., 2013, 2021; Phukon et al., 2018; Phukon, 2022; Hifzurrahman et al., 2021, Patel et al., 2025).

Understanding the tectonic evolution of NICM is crucial for elucidating the assembly of the Columbia supercontinent in South Asia. Debates persist regarding (i) the nature of NICM as active margin (based on the presence of subduction-related Proterozoic granitoids along the Himalayan belt, Phukon, 2022; Pandey, 2022) versus passive margin (based on the Lesser Himalayan rocks in the Central Himalaya, such as those in Nepal and parts of India including Nawakot Group of formations such as the Proterozoic Kuncha turbidites of 1900 Ma, Fag fog quartzites of 1770–1790 Ma, and Syangja volcano-sedimentary sequence of 1750 Ma, Brookfield, 1993; Myrow et al., 2003) (ii) its paleogeographic correlations (Phukon, 2022; Pandey, 2022; Rogers and Santosh, 2002; Zhao et al., 2004) and uncertainties surrounding the subduction dynamics of the proto-NICM, including whether it involved continuous subduction, double subduction, or the accretion of multiple island arcs, and its paleogeographic correlations with East Antarctica, the North China Craton, and other Gondwanan elements (Meert, 2012), (iii) the connection between the Central Indian Tectonic Zone and Columbia, as well as NICM (Vansutre and Hari, 2010; Rekha and Bhattacharya, 2014; Bhowmik, 2019; Chattopadhyay et al., 2020; Chakrabarty et al. 2023; Sethy et al., 2025), (iv) the obscurities of Proterozoic NICM features by the Himalayan orogeny, thus complicating tectonic reconstructions from the Columbia era (Searle, 1996), and (v) the timing and tectonic implications of Proterozoic crustal extension events in the NICM (Mishra and Ravi Kumar, 2014; Sen et al., 2019; Phukon, 2022), which are critical for understanding its role in Columbia's assembly.

Proposed connections between NICM, Lesser Himalaya, Aravalli

Craton, and the Cathaysia Block are based on similarities in their metamorphic histories as well as basin evolution (Auden, 1935; Gansser, 1964; Valdiya, 1976; Bhargava, 2000; Richards et al., 2005; McQuarrie et al., 2008; Long et al., 2011; Spencer et al., 2012; Yu et al., 2012; Wang et al., 2018, 2019 and 2021; Cawood et al., 2020). The Almora Nappe and associated klippen of Kumaun provide significant insights into these relationships (Valdiya, 1980). Therefore, investigating the Lesser Himalaya is essential not only for elucidating the Proterozoic geodynamic evolution of the NICM, but also for establishing paleogeographic spatial and temporal linkages between Indian Craton and other Columbia fragments. By examining these ancient metamorphic records, we can better constrain the timing, processes, and thermal regimes that governed continental accretion and stabilization during Columbia's formation.

In this paper, we investigate high-grade metapelitic rocks from the Askot Klippe (Lesser Himalaya, India) to unravel their polymetamorphic tectono-thermal evolution and assess their significance within the NICM in the context of Columbia supercontinent assembly. We present new petrological and U–Pb zircon geochronological data to constrain their Paleoproterozoic metamorphic history. Our approach integrates conventional and high-resolution thermobarometry, isochemical phase diagram modelling, together with detailed textural and mineral assemblage analyses, and whole-rock geochemistry, to reconstruct their pressure–temperature (P–T) evolution. The resulting P–T path is

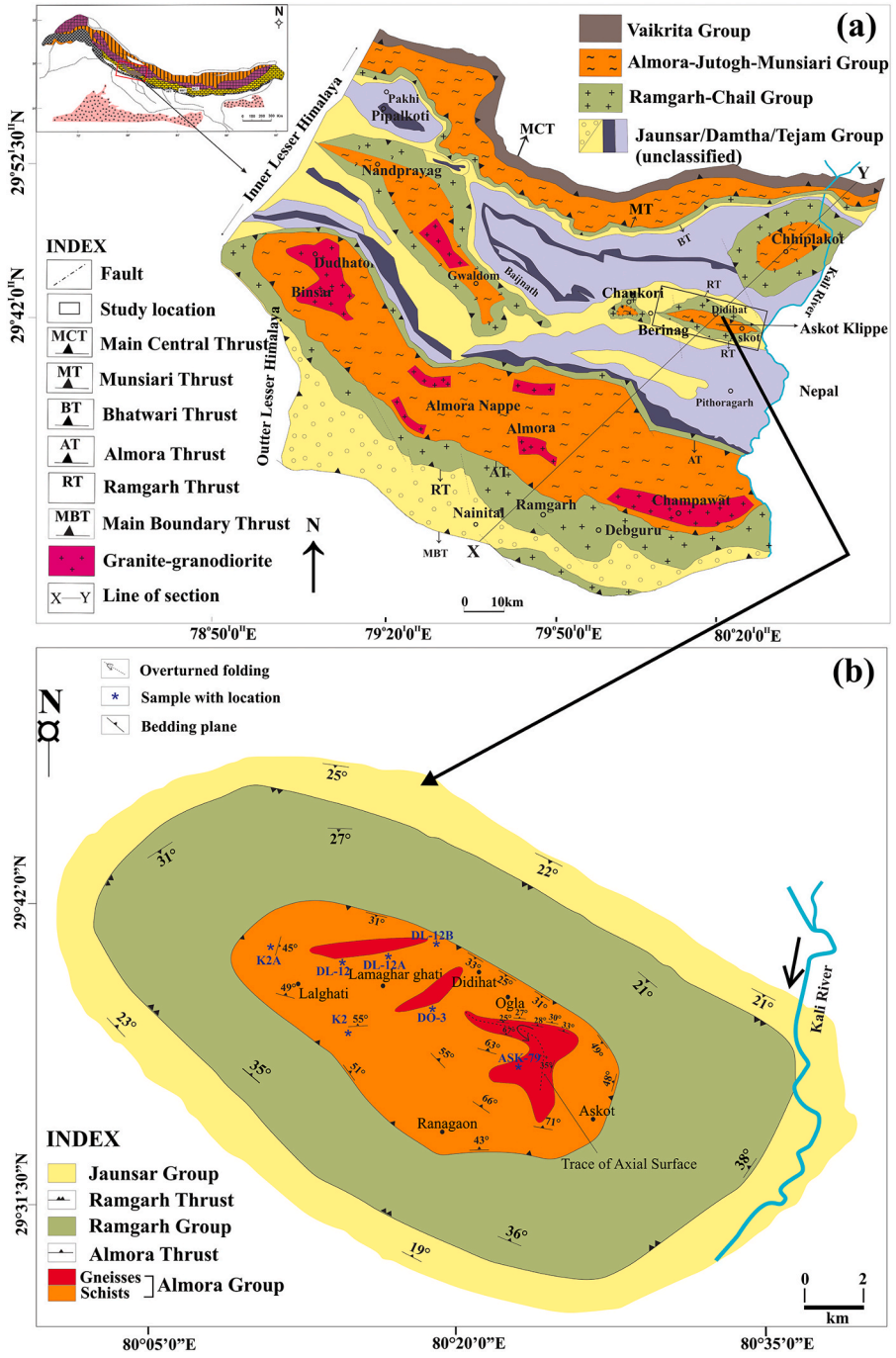

Fig. 1. Simplified tectonic diagram of Askot Klippe. (a) Regional geological map of the eastern Kumaun Himalaya. Rectangular box shows the location of the study area (modified after Valdiya 1980). XY is the section line for the cross section shown in Fig. 2a, b. Simplified geological map of the Askot Klippe showing different thrust contacts and the rock types (modified after Das et al. 2019).

compared with those from other Himalayan regions to evaluate regional metamorphic patterns. Finally, we explore tectono-metamorphic and geochronological correlations between the Askot Klippe and other Paleoproterozoic terranes of the NICM, providing new insights into their potential paleogeographic linkages during Columbia's assembly.

2. Geological background

2.1. Regional geology and tectonic setting

As a consequence of the crustal shortening during the Cenozoic Himalayan Orogeny (Molnar and Tapponier, 1975; Srivastava and Mitra, 1994; Patzelt et al., 1996; Joshi, 1999; Searle, 1986; Joshi et al., 2019), the lowermost units of the High Himalaya were thrust southwards over the Lesser Himalayan sedimentary rocks and the remnants of this large thrust sheet occur as nappes and klippen strewn all over the Himalayan strike. One of these klippen, the Askot Klippe, comprises Ramgarh Group as its lithotectonic base and the overthrust Almora Group as its metapelitic cover (refer Fig. 1a, 1b of present work, see Das et al., 2019; Das et al., 2021 for detail information therein). The Almora Group is correlated with the Munsiari Group of the High Himalayan Metamorphics following Valdiya (1980). The rocks of both the Almora and Munsiari Group are sequences comprising interbanded metapelites and *meta*-psammites with marked similarity in the tectonic and metamorphic textural-mineralogical details.

The Almora Group and its equivalent klippen including the Askot Klippe comprise medium-to-high grade metapelitic rocks and the degree of shearing decreases up section towards the central part (Das et al., 2019). The lithotectonic setting of the klippe is notably similar to the Almora Nappe (Joshi, 1999; Joshi and Tiwari, 2007, 2009). The prograde sequence in the Almora Group rocks in the Askot Klippe comprises low-to-high-grade metapelitic schists and gneisses. The metapelites are interspersed with quartzite bands of varying dimensions and the metamorphosed pelite-psammite sequence shows notable similarity with the analogous metamorphosed rock sequence in the Almora Nappe.

2.2. Field observation and sample descriptions

We carried out detailed field investigations, including lithological and structural mapping, of the Almora Group metapelites in the Askot Klippe. We took several traverses from the base to the central part of the klippe across the strike of the klippe. Our field investigations revealed four distinct prograde metamorphic zones, starting with chlorite-biotite bearing metapelitic schists of greenschist facies at the base of the klippe to progressively higher-grade assemblages of garnet-sillimanite-K-feldspar-bearing metapelitic gneisses that reached upper amphibolite to granulite facies transition conditions (see Supplementary Table S1 for sample locations). We identified four metamorphic zones and isograds with antiformal dispositions (Fig. 2a, 2b), namely, the chlorite-biotite zone (sample DL-12B, Fig. 3a), garnet-biotite zone (samples DL-12A and K2A, Fig. 3b), kyanite-biotite zone (samples K2 and DL-12, Fig. 3c), and K-feldspar-sillimanite zone (samples ASK-79 and AS-8, Fig. 3d). Reaction isograds, based on petrologically constrained mineral assemblages and metamorphic reactions, separate each zone.

The chlorite-biotite zone is characterized by the phyllites and biotite schists of the Almora Group. Phyllites with greenish appearance crop out around the Didihat region in the NW of Askot town. Chlorite and sericite are the predominant minerals in phyllites. Muscovite, chlorite, brown biotite and quartz are among the major phases and the phyllites contain numerous quartz veins that are observed in the Didihat-Ogla traverse. The garnet – biotite zone characterized by the garnet-mica schists is exposed between Didihat and Askot. Pelitic mica-schists (Fig. 3a, 3b) exposed in the peripheral parts of the Almora Group are followed upsection by kyanite-garnet-mica schists (Fig. 3c) and garnet-sillimanite-K-Feldspar gneisses (Fig. 3d) in the nappe due to folding. The presence of kyanite and sillimanite is not abundant, likely due to

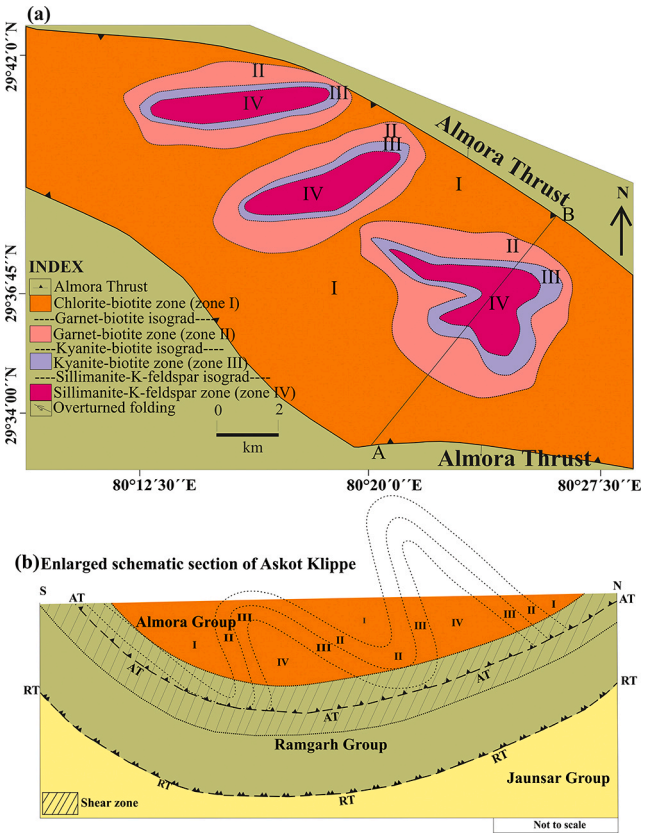

Fig. 2. (a) Isograd map of the area showing the disposition of different metamorphic zones (modified after Joshi et al. 2018); (b) Enlarged schematic section of the Askot Klippe showing the disposition of metamorphic zones and corresponding rock types in an antiformal disposition. Colours and symbols are taken from Fig. 2a.

compositional factors in the parent rocks. These garnet-kyanite bearing schists are occasionally traversed by quartz veins. At the highest metamorphic grades, the kyanite schists are succeeded by the metapelitic gneisses of the sillimanite-K-feldspar zone, occasionally through migmatites, which show alternate lighter, irregular, vein-like bands of felsic materials as leucosomes and the dark, tightly folded layers as melanosome (Fig. 3e), which led to the development of the gneisses by prograde metamorphism that underwent partial melting at peak conditions.

3. Methods and techniques

Thin sections of metapelitic schists and gneisses were cut perpendicular to the dominant foliation and further polished for both the petrological studies and probe analysis to capture the cross-sectional views of the metamorphic reaction textures and mineral parageneses. The mineral chemistry of representative minerals was carried out using the Electron Probe Micro Analyzer (EPMA) CAMECA SX-Five at the Centre of Advanced Study in Geology, Institute of Science, Banaras Hindu University (see Supplementary Table S2). The garnet crystals were analyzed by taking rim-to-rim chemical line profiles to distinguish the core and the rim. Polished thin sections were coated with 20 nm thin layer of carbon for electron probe micro analyses using the LEICA-EM ACE200 instrument. The EPMA was operated at a voltage of 15 kV and filament current of 10nA with a LaB6 source in the electron gun for the generation of the electron beam. Natural silicate mineral andradite as internal standard was used to verify positions of crystals (SP1-TAP, SP2-LiF, SP3-LPET, SP4-TAP and SP5-PC1) with respect to corresponding wavelength dispersive (WD) spectrometers (SP#) in CAMECA SX-Five instrument. The following X-ray lines were used in the analyses:

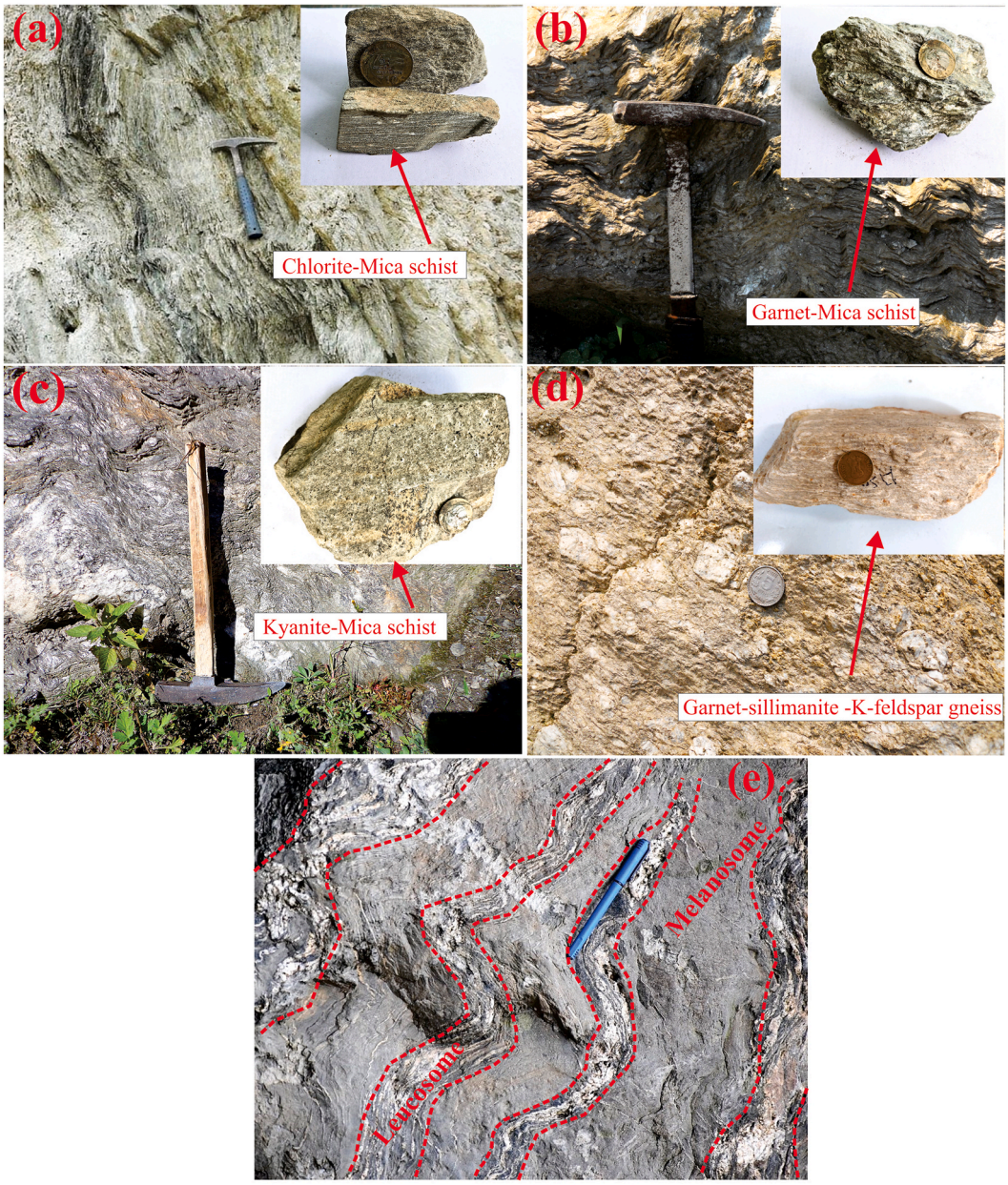

Fig. 3. Field photographs of Almora Group. a. Chlorite-Mica bearing metapelitic schist; b. Garnet-Mica bearing metapelitic schist; c. Kyanite-Mica bearing metapelitic schist; d. Garnet-Sillimanite-K-Feldspar bearing metapelitic gneiss; e. Presence of migmatite showing leucosomes (melt-derived portion) and melanosome (original metamorphic rock).

F-*Kα*, Na-*Kα*, Mg-*Kα*, Al-*Kα*, Si-*Kα*, P-*Kα*, K-*Kα*, Cl-*Kα*, Ca-*Kα*, Ti-*Kα*, Cr-*Kα*, Mn-*Kα*, Fe-*Kα*, Ni-*Kα*, and Sr-*Lα*. Natural mineral standards: apatite, albite, halite, periclase, peridote, corundum, wollastonite, orthoclase, rutile, chromite, rhodonite, celestite, barite, hematite and synthetic Ni metal supplied by CAMECA-AMETEK used for routine calibration and quantification. Routine calibration, acquisition, quantification and data processing were carried out using Sx-SAB version 6.1 and SX-Results software of CAMECA. Elemental mapping was also performed on the garnet crystals to know the spatial distribution of each element.

Both the metapelitic schists and gneisses of the Almora Group from the Askot Klippe were selected for bulk analysis using the X-ray Fluorescence (XRF) Spectrometer (Make/Model: Bruker S-8 Tiger) at the Wadia Institute of Himalayan Geology, Dehradun, India (see Supplementary Table S3). The instrument was operated at a voltage of 20–40 kV. A total of 15 kg of the selected samples are ground into fine powder to the size consistency of ~200 μ. From each powdered sample, only 8–10 g of pressed powder pellets is taken for the final measurement. As H_2O is a major constituent and can't be measured directly by XRF, hence 1–2 g of each dried rock powder is ignited in alumina crucible at 950°C for about one hour to get the weight % of H_2O in the form of Loss on Ignition (LOI). For measuring the calibration, a range of crystals, namely GA, G-2, GSP-1, AGV-1, JG-2, JA-2, and DG-H were used as standard with the analytical accuracy better than 5% for major oxides and the precision in terms of maximum observed standard deviation on repeated measurements is always better than 1.5% (Saini et al., 1998).

The possible *P-T* modeling of a metamorphic terrain can be deduced by the mineral chemistry of a rock sample by the approach of forward and inverse thermodynamic modelings (Lanari and Duesterhoeft, 2019). To obtain precise pressure–temperature (P-T) estimates, it is essential to analyze fresh garnet crystals exhibiting the largest diameters and depicting no evidence of chemical weathering or leaching, as these features preserve pristine chemical zoning and minimize diffusive re-

equilibration that could obscure the original metamorphic history of these rocks.

For high-resolution P-T path modeling and conventional geothermobarometry, three representative samples were selected: one sample from metapelitic schist (DL-12) and two samples from metapelitic gneisses (AS-8 and ASK-79). These samples were chosen because they contain well-preserved, unweathered garnets with larger diameters exceeding 1 mm, ensuring reliable garnet P-T path modeling and reaction equilibria calculations; additionally, their mineral assemblages and bulk compositions align with regional metamorphic gradients, allowing robust reconstruction of prograde and retrograde paths.

In contrast, for constructing isochemical phase diagrams, a subset of these samples was used: one sample from metapelitic schist (DL-12) and the two samples from metapelitic gneisses (AS-8 and ASK-79). This selection was justified by the samples' distinct bulk rock compositions, to effectively capture the stability fields of peak metamorphic assemblages (e.g., garnet + biotite + sillimanite + K-Feldspar + cordierite in the gneisses, and garnet + biotite + kyanite in the schist), as corroborated by detailed petrographic observations of textural equilibrium and phase relations.

Isochemical phase diagrams were computed for the measured bulk rock compositions using Perple_X (version 7.1.1) (Connolly, 2005) for the model system Na_2O-CaO-MnO-K_2O-FeO-MgO-Al_2O_3-SiO_2-H_2O-TiO_2 (MnNCKFMASHT) to decipher the stability of various phases in the studied rock types. The CORK fluid equation of state (Holland and Powell 1991, 1998) was used for the saturated fluid components. The amount of H_2O analyzed in the XRF analysis was used as the 'loss on ignition' (LOI) value for calculations of isochemical phase diagrams. The solution models of White et al. (2014) adopted for these zones are Bi (W), Gt (W), Crd (W), Chl (W), Ctd (W), Mica (W), Ilm (WPH), melt (W) and feldspar (see Supplementary Table S4). T-XH_2O phase diagrams were computed for the measured bulk rock compositions to estimate the actual water content present in the rock during metamorphism. Modified phase diagrams were constructed using Effective Bulk Composition (EBC) calculated by using the approach of Evans (2004) and Gaidies et al., (2006) based on the Rayleigh fractionation principle to demonstrate the effect of fractionation on stability of different phase assemblages.

In the Zircon U-Pb geochronological technique, zircon grains were separated from ~7 kg of sample by crushing and sieving up to 250 μm followed by gravity (Holman Wilfley water table), magnetic and heavy liquid separations. About 70 zircon grains were handpicked under a binocular microscope and mounted on per-fluoro-alkoxy alkaline (PFA ®) teflon sheet followed by polishing to expose the mid-section. Cathodoluminescence (CL) imaging of the zircon grains was carried out using Zeiss EVO 40 extended pressure (EP) scanning electron microscope (SEM) at the Department of Geology, Banaras Hindu University, Varanasi, India to study the internal structure and selecting locations for U-Pb analysis. A multi-collector inductively coupled plasma mass spectrometer (MC-ICPMS; Neptune Plus, Thermo Fisher Scientific) with a 193 nm excimer laser ablation system (UV Lase, Model Analyte G2, Cetec-Photon machine) was used for zircon U-Pb dating at Wadia Institute of Himalayan Geology, Dehradun, India. Instrumental conditions and analytical procedures were similar to those described by Mukherjee et al. (2017). Spot diameter of 25 μm, 67.5% laser intensity, repetition rate of 5 Hz and an energy density of 3.5 J/cm^2 were applied for the analysis. Zircon standard Z91500 was used as the primary standard (Wiedenbeck et al., 1995), and the standard silicate glass NIST 610 was used to optimize the machine. The accuracy was later checked using the zircon standard Plešovice (Slama et al., 2008) as the external standard. The standard zircon was analyzed first and then after every 10 unknowns. Isotopic ratios and elemental compositions of zircon were processed using Iolite software (Paton et al., 2011). Concordia diagrams and weighted mean age calculation were plotted using Isoplot R (Vermeesch, 2018). The uncertainties for individual spot analysis are presented at 2σ, and intercept ages are also quoted at 2σ (95% confidence level). The analytical results of zircon U-Pb ages are listed in Supplementary Table S5.

4. Results

4.1. Reaction textures

4.1.1. Chlorite-biotite zone

The phyllitic schists are characterized by the presence of chlorite, muscovite, biotite, plagioclase, and quartz. The minerals observed in this zone are fine-grained and the foliation is defined by the preferred alignment of chlorites and larger mica flakes (Fig. 4a). The lepidoblasts of Mg-rich chlorite in this zone follow the major foliation trend. Cross-cutting muscovites of at least two generations are present (Fig. 4b), where older generations of muscovite are observed to cut the younger muscovite flakes at varied angle.

4.1.2. Garnet-biotite zone

The onset of the garnet-biotite zone is marked by the development of garnets having size range of 500 μm to 1500 μm (Fig. 4c) by the reaction Chlorite + Muscovite + Quartz = Garnet + Biotite + Water. Two generations of garnet porphyroblasts, namely $garnet_1$ and $garnet_2$ are identified. Around the rim of the earlier-formed garnet, there are numerous quartz inclusions present. Persistent association of garnet porphyroblasts and biotite flakes characterizes the stable garnet-biotite association. Small prism-shaped zircon crystals having higher relief are observed as a pleochroic halo in biotites (Fig. 4d). The instability is clearly observed in this zone due to the corroded boundary between garnet and muscovite. A neutral pressure shadow with a crude 'S'-shaped inclusion trails of quartz is developed around garnet porphyroblasts (Fig. 4e). A fractured, relict, and resorbed grain of garnet is surrounded by thin coatings of hematite (Fig. 4f).

4.1.3. Kyanite-biotite zone

This zone is characterized by scattered garnet idioblasts in a matrix of muscovite, biotite, and chlorite. Kyanite blades having high relief and upper 1st order interference colour and size range of around 180–220 μm (Fig. 5a) occur in close association with biotite flakes likely by the reaction garnet + muscovite = biotite + kyanite + quartz. Here, laths of muscovite observed in the zone define the major foliation plane.

4.1.4. Sillimanite-K-feldspar zone

This zone is characterized by the presence of garnet cordierite, sillimanite needle, K-feldspar, muscovite, and biotite. The intergrowth of plagioclase and K-feldspar shows perthitic texture in this zone (Fig. 5b). This texture can be treated as the petrographic manifestation of liquid immiscibility in the studied rock.

The reaction boundaries of muscovite-plagioclase-quartz (Fig. 5c and 5d) are corroded and invariably fuzzy and discolored, which leads to the reaction of muscovite + plagioclase + quartz = Al_2SiO_5 + K-feldspar + melt (Evans and Guidotti, 1966; Thompson and Algor, 1977; Patino-Douce and Harris, 1998). The presence of thin sillimanite needles in association with K-feldspar is inferred to have formed by the above reaction (Fig. 5e). The cordierite seen around garnet rim (Fig. 5f) is reported for the first time from any of the nappes and klippes of the Lesser Himalaya.

4.2. Mineral chemistry

Compositional zoning profiles, BSE image and X-ray elemental map of representative garnet was analyzed by EPMA for both the metapelitic schists and gneisses of Almora Group (Fig. 6). We took the zoning data of garnet analyzed by EPMA, where X_{Ca} is defined by Ca/(Ca + Mg + Fe + Mn), X_{Mg} is defined by Mg/ (Fe + Mg + Ca + Mn), X_{Fe} is defined by Fe/ (Fe + Mg + Ca + Mn) and X_{Mn} is defined by Mn/(Ca + Mg + Fe + Mn). The compositional plot of garnet of both metapelitic schists and gneisses

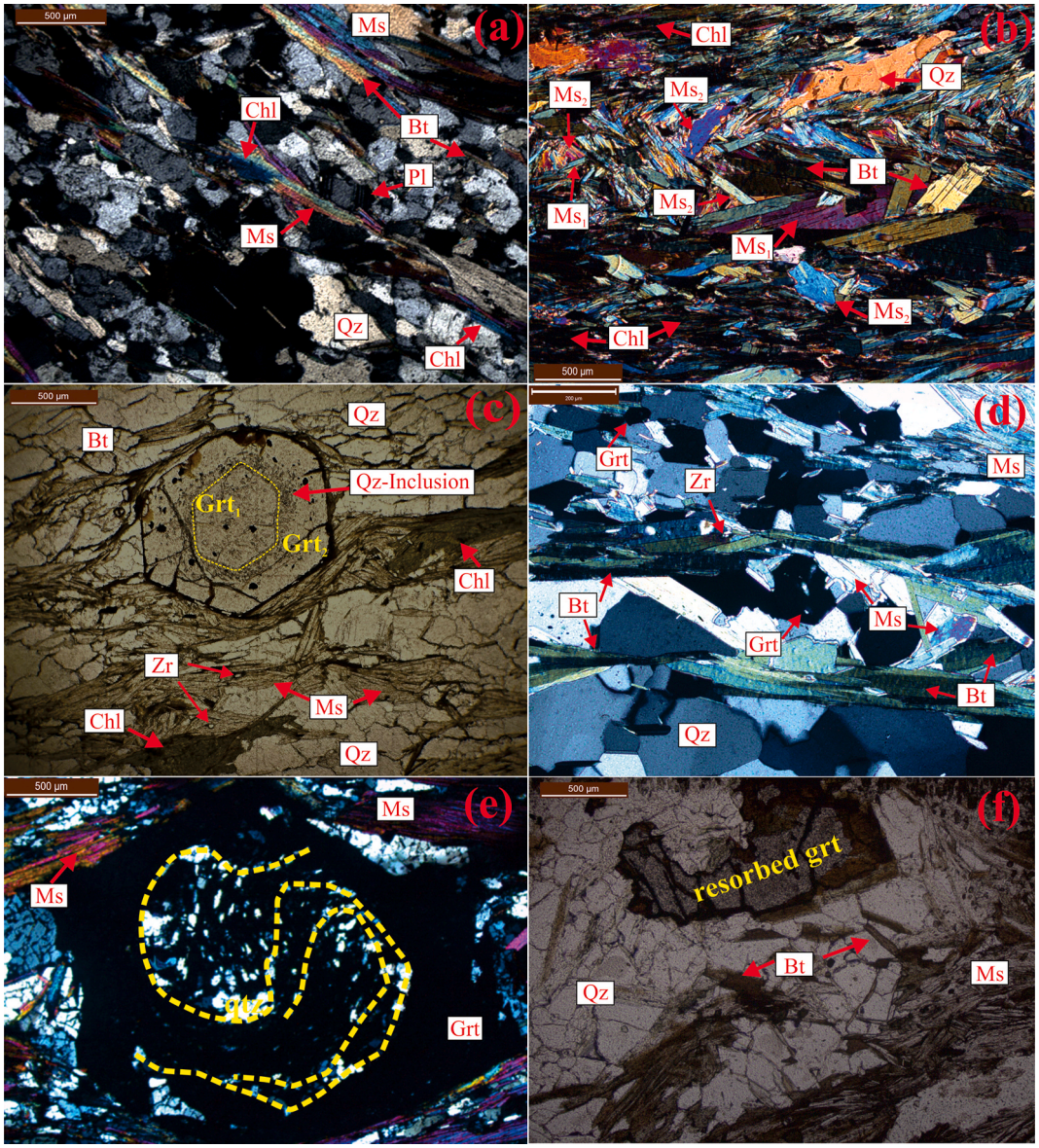

Fig. 4. (a) Presence of chlorite, biotite, muscovite, albite and quartz and preferred alignment of mica lepidoblasts along the regional foliation plane. Note that the chlorite, and mica define the regional foliation plane; (b) Presence of two generations of mica, which are observed to cut across each other at varied angle to the regional foliation plane; (c) Presence of garnet-in-garnet association with numerous inclusions of quartz around earlier garnet rim; (d) Unstable garnet-muscovite contact. Note the pleochroic halo of zircon in biotite; (e) S-shaped inclusion trail within garnet; (f) Presence of relict and resorbed garnet. Mineral abbreviations (Grt = Garnet; Pl= Plagioclase; Ms = Muscovite; Bt = Biotite; Qz = Quartz; Chl= Chlorite; Zr = Zircon) are after Whitney and Evans (2010).

shows the profile of Ca, Mg, Mn, and Fe from rim to rim. The zoning profiles and X-ray elemental maps for samples DL-12 and AS-8, derived from electron microprobe analyses and mapping, reveal typical growth zoning patterns. The profiles indicate a single prograde growth episode with minimal diffusive re-equilibration, preserved due to relatively rapid burial/exhumation rates during the metamorphism. For the sample DL-12, the garnet exhibits classic prograde "Christmas tree" zoning, with a Mn-rich core and Fe-Mg enriched rim. The crystal is subidioblastic (~1–2 mm diameter), with inclusions of quartz, biotite, and ilmenite concentrated in the core, suggesting nucleation during early garnet-in isograd conditions. In the compositional profile at 400 μm at the core, there is Low-T nucleation followed by high Mn fractionation from the matrix. From 400 to 600 μm from the core to rim, temperature increases with Mn depletion in the matrix. From 600 to 800 μm, rise in X_{Mg} indicates 'Mg' availability from biotite breakdown, garnet sustains peak equilibrium conditions with matrix. Sharp decrease in X_{Mn} reflects temperature-dependent partitioning. X_{Fe} and X_{Mg} increases suggesting prograde heating and reaction progress which is evident by the reaction chlorite + muscovite → biotite + garnet. X_{Ca} remains low (15–10 mol%) from core to rim, typical for Ca-poor pelites. Concentric bands show a brighter X_{Mn} core (reddish core) fading to a dark rim, with Mg intensity increasing outward from darker blue to brighter blue. X_{Fe} is nearly homogeneous (dull yellow to brighter yellow). In case of sample AS-8, compositional zoning is similar but more subdued, with a slightly larger garnet crystal. The compositional profile at 0 μm at the core is attributed to initial growth with slightly lower Mn than DL-12. The compositional variation from 1000 to 1500 μm across the core-to-rim section is characterized by a steady garnet growth. The variation from 1500 to 1700 μm, suggests peak thermal conditions. X_{Mn} decreases more gradually than in DL-12, attributed to kinetic effects during the rapid growth of garnet. X_{Ca} shows a weak bell-shaped profile, which is very common in the metapelitic gneisses of Himalayan fold-thrust belt (see Joshi and Tiwari, 2009; Das et al., 2019 for detailed analyses) with minor calc-silicate influence, indicating localized Ca

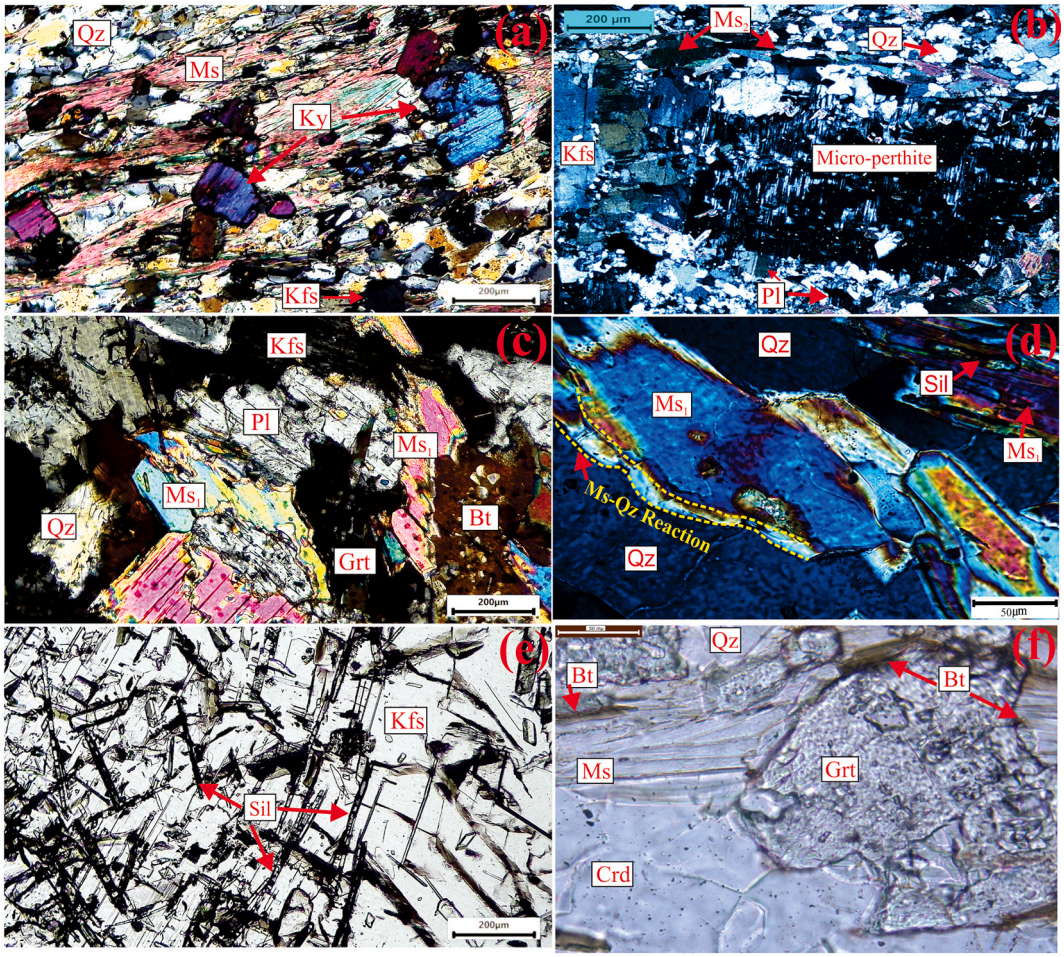

Fig. 5. Photomicrographs of sillimanite-K-feldspar zone of the garnet-cordierite-sillimanite-K-feldspar bearing metapelitic gneisses, Almora Group. a. Presence of kyanite in association with muscovite, quartz, and K- feldspar; b. Presence of micro-perthite showing intergrowth of plagioclase and K- feldspar; c, d. corroded boundary between muscovite, plagioclase and quartz suggesting disequilibrium conditions between these mineral pairs and initiation of dehydration melting reaction, muscovite + plagioclase + quartz = K-feldspar + sillimanite + melt; e. Needles of sillimanite in association with K- feldspar; f. Garnet-cordierite association. Mineral abbreviations (Grt = Garnet; Kfs = K-feldspar; Pl= Plagioclase; Ms = Muscovite; Bt = Biotite; Qz = Quartz; Crd= Cordierite; Chl= Chlorite; Sil= Sillimanite; Ky = Kyanite) are after Whitney and Evans (2010).

enrichment during exhumation. Similar concentric X_{Mn} depletion (reddish yellow core to darker blue rim) in X-ray elemental map of AS-8 with patchy X_{Mg} increase (darker blue core to lighter blue rim) and faint X_{Ca} compositional variation occurs near the rim. Mn map shows subtle irregularities, reflecting sector zoning, while X_{Fe} is uniform, which confirms minimal retrograde diffusion.

4.3. *High resolution P-T path using 'Theriak' combined with MATLAB program*

The P-T path modeling was computed (Fig. 7) for three representative samples (DL-12, ASK-79, and AS-8) using the Theriak-Domino software (De Capitani and Brown, 1987; De Capitani and Petrakakis, 2010) in conjunction with MATLAB program by the automated routine of Moynihan and Pattison (2013).

The modeling was carried out using bulk rock compositions (See supplementary Table S3) with the thermodynamic data set of Holland and Powell (1998) with updated solution models through 2003 and 2011, and selective solution models in the system Na_2O-CaO-MnO-K_2O-FeO-MgO-Al_2O_3-SiO_2-H_2O-TiO_2 (MnNCKFMASHT). The thermodynamic assumptions inherent in this approach are the same as Moynihan and Pattison (2013). Some of the key assumptions made in this modeling approach are; (1) the local equilibrium conditions of garnet growth, with mineral assemblages and compositions stable and in equilibrium with the surrounding matrix at each P-T step of the modeling, (2) Equivalence of observed and modelled zoning profile of garnet, (3) 100% fractional crystallization of garnet with no resorption, back-reaction, or internal metasomatism, and equivalence of matrix compositions with the Effective Bulk Composition (EBC), (4) Assumption of excess H_2O, implying a pure H_2O fluid phase in equilibrium with the rock (fluid-saturated condition), and (5) Exclusion of partial melting, assuming sub-solidus conditions throughout garnet growth, limiting its applicability to rocks below wet-solidus. Based on the chemical data, we assumed the highest Mn content of the garnet as the 'core'. We took the largest garnet crystal assuming that the garnet having the largest dimension would preserve the representative *P-T*. The purpose of this modeling is to correspond to the modal garnet end-member compositions from the core-rim transect with the observed garnet end-member compositions from the modeling to deduce the P-T conditions.

The Theriak P-T path with MATLAB script was run using the EPMA compositional data of garnet transect and bulk rock compositional data from XRF to compute appropriate *P-T* conditions of the rock. The program was executed successfully to retrieve the *P-T* conditions for each sample. The sample DL-12 yielded a *P-T* of 0.42 GPa/524°C at the core and 0.58 GPa/572°C at the rim; sample ASK-79 yielded a *P-T* of 0.54 GPa/539°C at the core and 0.63 GPa/591°C at the rim; sample AS-8 yielded a *P-T* of 0.43 GPa/526 °C at the core and 0.63 GPa/566 °C at the rim (see supplementary Table S6). It is needless to mention here that

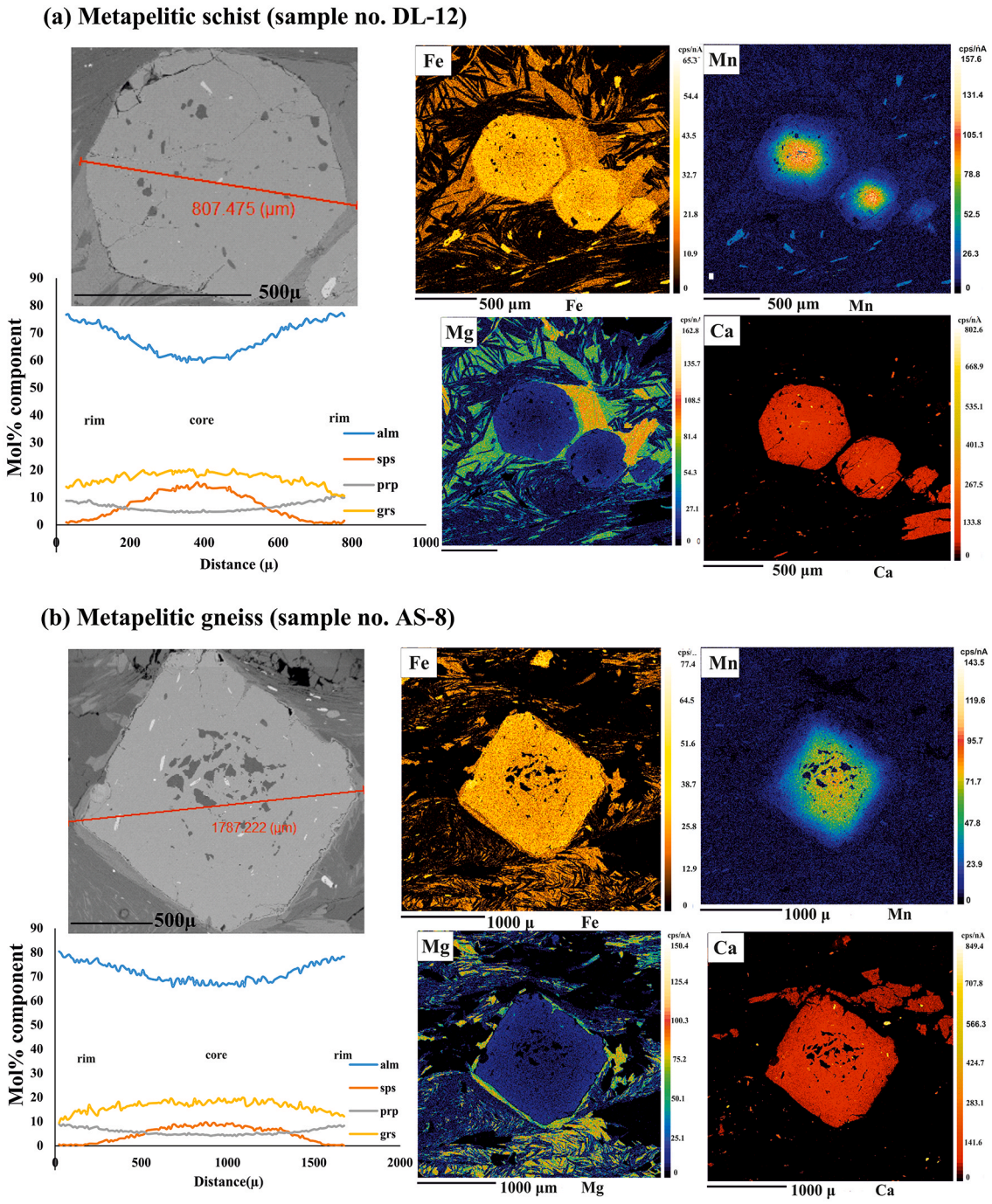

Fig. 6. X-ray elemental map, BSE image and zoning profile of garnets in metapelitic schists (a) and gneisses (b) of the Almora Group. Colour palette: Mg, darker blue (lower concentration) – lighter blue (higher concentration); Fe, darker yellow (lower concentration) – lighter yellow (higher concentration); Mn, darker yellow (higher concentration) – blue (lower concentration); Ca, lighter red (higher concentration) – patchy red (lower concentration).

reported P-T conditions from this modeling arise primarily from the program's computational methodology, which depends on Gibbs free energy minimization to derive equilibrium states, based on the model's assumptions, not rounded or adjusted for uncertainty. Explicitly, typical uncertainties in this case are around ±50°C for temperature and ±0.2 GPa for pressure, which can be estimated using methods like Monte Carlo simulations or error propagation, to reveal the output shift by small input variations. The measures of uncertainties due to the several key sources, viz., analytical errors in input data, limitations in thermodynamic databases, approximations in mixing parameters for solid solutions of garnet and biotite, assumptions like perfect equilibrium, closed/open system behavior, and change in overall bulk composition of rocks (Palin et al., 2016) cannot be ruled out.

4.4. *P-T path by conventional thermobarometry*

The temperature and pressure for both the core and rim were calculated using different thermobarometric models and the *P-T* were calculated for the chlorite-biotite zone, garnet-biotite zone, kyanite-biotite zone, and sillimanite-K-feldspar zone using conventional thermobarometry (Thompson 1976; Holdaway and Lee, 1977; Ferry and Spear, 1978; Hodges and Spear, 1982; Perchuk et al., 1985; Perchuk and

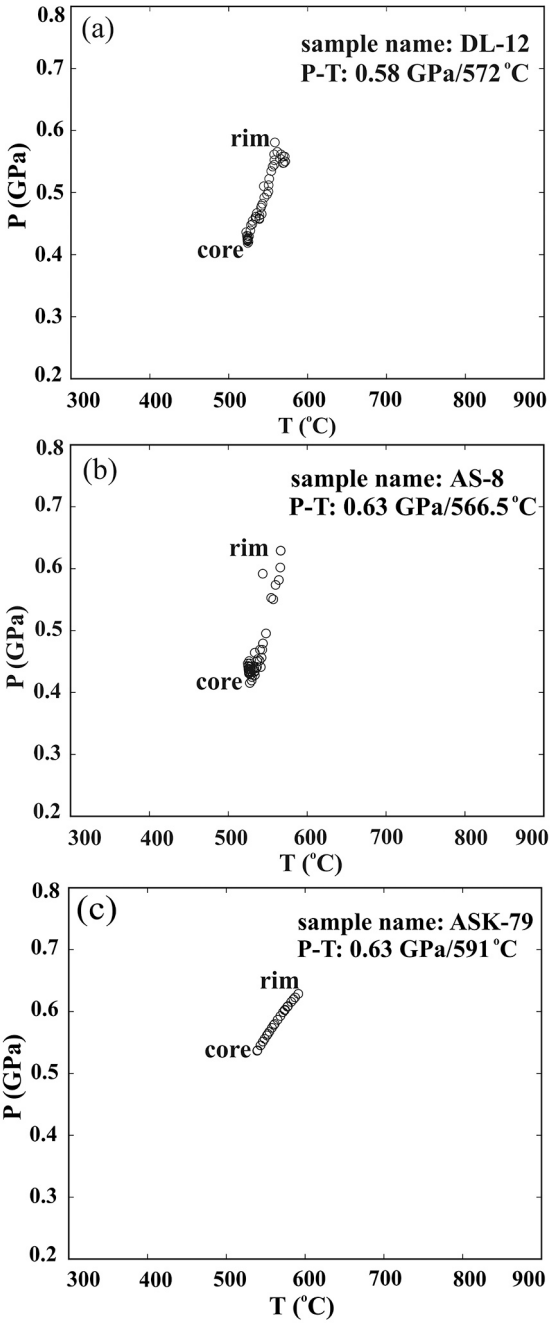

Fig. 7. High resolution P-T path of representative samples using Theriak-Domino in conjunction with MATLAB program. (a) core-rim P-T conditions of sample no. DL-12; (b) core-rim P-T conditions of sample no. AS-8; (c) core-rim P-T conditions of sample no. ASK-79.

Lavrent'eva, 1983; Dasgupta et al., 1991; Holdaway, 2000). Garnet core + biotite inclusions with no reaction rims represent prograde conditions; garnet rim and matrix biotite with equilibrium and no retrogression textures represent peak conditions; and matrix garnet-plagioclase-muscovite-biotite with post-peak breakdown represent retrograde conditions. All pairs were selected from equilibrium assemblages confirmed by BSE imaging and EMPA. The average temperatures estimated for the core-rim of samples DL-12 and AS-8 by applying garnet-biotite geothermometer are 422°C–494°C for the chlorite-biotite zone; 436°C–528°C for the garnet-biotite zone; 454°C–556°C for the kyanite-biotite zone and 689°C–745°C for the sillimanite-K-feldspar zone. The sample ASK-79 yielded a core-rim temperature of 648°C–725°C for the sillimanite-K-feldspar zone. For the estimation of pressure in both the metapelitic schists and gneisses, the Garnet-Biotite-Plagioclase-Quartz (GBPQ) geobarometer (Wu et al., 2004) and the GASP geobarometer (Holdaway, 2001) were used. For GBPQ and GASP geobarometry, co-existing pairs of Garnet-Biotite-Plagioclase-Quartz in equilibrium assemblage without Al-silicate buffer, and Garnet-Plagioclase-Al_2SiO_5-Quartz in equilibrium were used to estimate the prograde, and peak pressure conditions. The average pressures estimated respectively for the core/rim are 0.35–0.52 GPa for the chlorite-biotite zone; 0.40–0.54 GPa for the garnet-biotite zone; 0.44–0.55 GPa for the kyanite-biotite zone and 0.61–0.66 GPa for the sillimanite-K-feldspar zone. A revised Ti-in-Biotite geothermometer experimentally calibrated by Wu and Chen (2015) for a pair of matrix ilmenite/rutile bearing biotite was used to estimate the peak temperature for the above zones of the metapelitic schists and gneisses by assuming Ti-saturation in biotite. A temperature of 477°C was calculated for the chlorite-biotite zone; 566°C for the garnet-biotite zone; 607°C for the kyanite-biotite zone and 746°C for the sillimanite-K-feldspar zone, with a propagated uncertainty of ±65°C raised through calibrations, analytical biasness, pressure estimation, and assumption of elemental Fe^{3+}. The matrix *P-T* conditions of 0.53 GPa and 571°C were estimated for the pair of matrix phases of Garnet-Plagioclase-Muscovite-Biotite in the metapelitic gneisses by employing GPMB-Fe geobarometer (Holland and Powell, 1998) and Garnet-biotite geothermometer (Aranovich et al., 1988). These P-T estimates were derived under the assumption of local chemical equilibrium within a closed system at the thin section scale, as evidenced by the systematic prograde compositional zoning preserved in garnet without indications of significant open-system behavior such as pervasive ingress of fluid, metasomatism, or veining. The sparse chlorite in the matrix suggests only minor retrograde hydration, further supporting predominantly closed-system behavior during peak and near-peak metamorphism. There are several measures of uncertainties in the P-T calculations, out of which most important sources may arise from calibration datasets, activity-composition models, analytical precision, and potential minor deviations from ideal equilibrium, viz., ±20–60°C for temperatures and ±0.10–0.15 GPa for pressures (see thermobarometric models of Holland and Powell, 1998; Holdaway, 2000, 2001; Wu et al., 2004; Wu and Chen, 2015).

4.5. Isochemical phase diagram modelling

4.5.1. Peak P-T phase diagram

Isochemical phase diagrams were calculated for the measured bulk composition from XRF using the Perple_X software package (Connolly, 2005) to constrain the peak pressure–temperature conditions and metamorphic evolution of representative metapelitic samples (DL-12, AS-8, and ASK-79) from the kyanite-biotite and sillimanite-K-feldspar zones (Fig. 8). The calculations use the internally consistent thermodynamic dataset of Holland and Powell (2011; hp62ver.dat file) and activity-composition models (White et al., 2014), with details of the models (supplementary Table S4). Phase diagrams with isopleth contour diagrams were constructed in a MnNCKFMASHT system using bulk-rock compositions. Uncertainties in P-T estimates incorporate analytical errors and dataset uncertainties (Holland and Powell, 2011). Key univariant reaction boundaries, viz., kyanite-sillimanite transition, melt-in, muscovite-out, and cordierite-in curves were contoured and superimposed on the diagrams to demonstrate the assemblage stability.

The phase diagram for kyanite-biotite zone was constructed for the sample DL-12 using measured bulk-rock composition within a P-T window ranging from 0.2 to 0.7 GPa and 300–700°C respectively (Fig. 8a). The diagram topology features divariant fields dominated by hydrous assemblages at lower grades, transitioning to Al_2SiO_5 polymorphs at mid-to-high temperatures. The prograde assemblages include muscovite-biotite-garnet-plagioclase-quartz evolving through peak mineral assemblages of garnet-muscovite-biotite-kyanite-feldspar-ilmenite-quartz, stable in the divariant field within a P-T range of

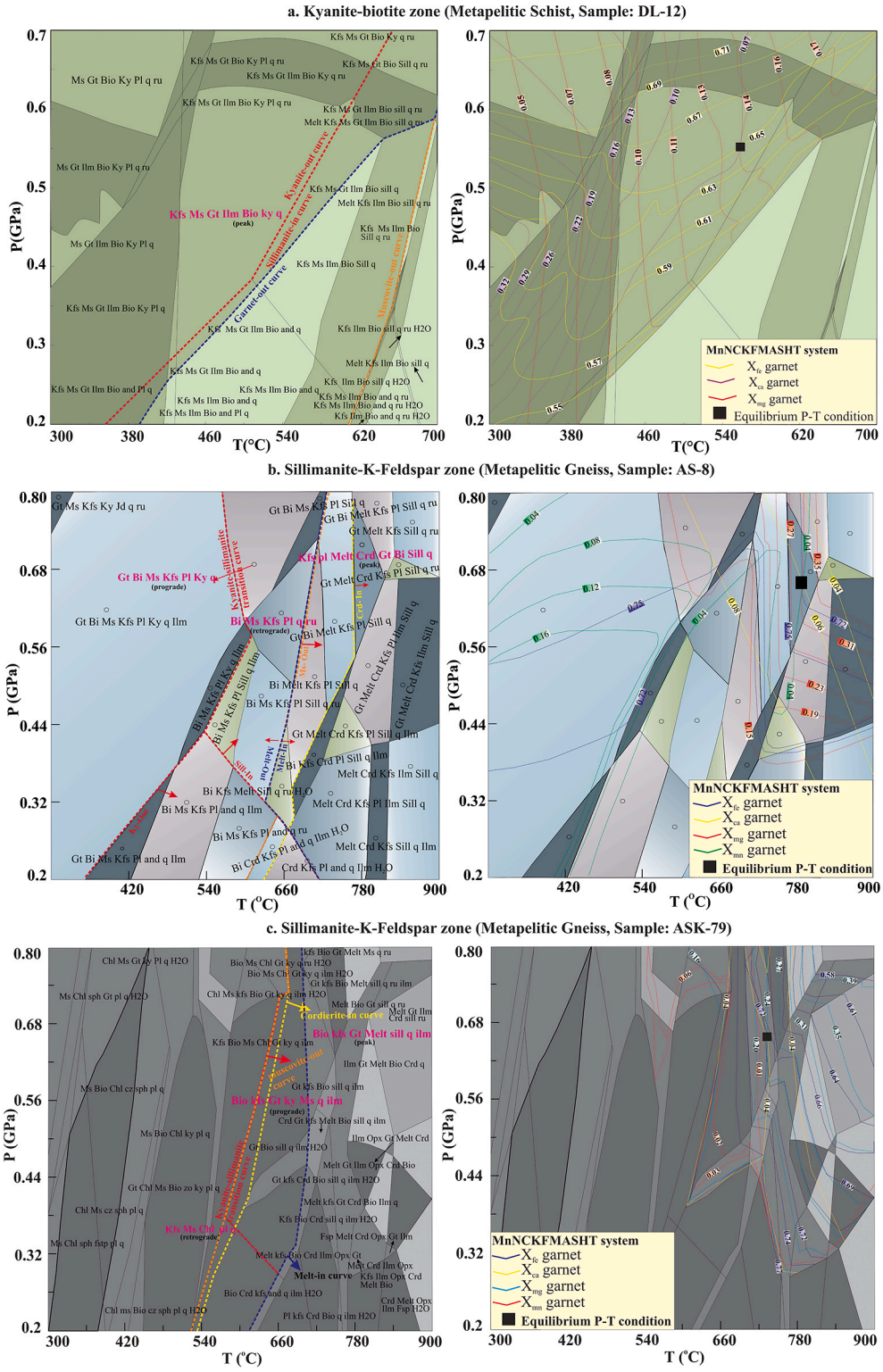

Fig. 8. A. isochemical phase diagram for the kyanite-biotite zone of the metapelitic schist (sample no. dl-12) in the mnnckfmasht system. the bulk composition in weight % from the xrf data are: na_2O 1.63, CaO 1.19, MnO 0.06, K_2O 4.68, FeOT 6.13, MgO 2.58, Al_2O_3 18.83, SiO_2 60.54, H_2O 1.75 TiO_2 0.80; The phase topology has been marked by kyanite-sillimanite transition curve, garnet-out curve, and muscovite-out curve, and has been contoured and intersected with the isopleths of garnet for the calculation of peak P-T conditions; b. Isochemical phase diagram for the sillimanite-K-feldspar zone of the metapelitic gneisses (sample no. AS-8) in the MnNCKFMASHT system. The bulk composition in weight % from the XRF data are: Na_2O 3.49, CaO 0.35, MnO 0.01, K_2O 3.52, FeOT 1.41, MgO 1.08, Al_2O_3 15.58, SiO_2 72.00, H_2O 2.31 TiO_2 0.13; The phase topology has been marked by kyanite-sillimanite transition curve, melt-in curve, cordierite-in curve, and muscovite-out curve, and has been contoured and intersected with the isopleths of garnet for the calculation of peak P-T conditions; c. Isochemical phase diagram for the sillimanite-K-feldspar zone of the metapelitic gneisses (sample no. ASK-79) in the MnNCKFMASHT system. The bulk composition in weight % from the XRF data are: Na_2O 1.27, CaO 0.70, MnO 0.04, K_2O 3.72, FeOT 9.23, MgO 3.80, Al_2O_3 19.07, SiO_2 55.72, H_2O 6.68 TiO_2 0.85; d. The phase topology has been marked by kyanite-sillimanite transition curve, melt-in curve, cordierite-in curve, and muscovite-out curve, and has been contoured and intersected with the isopleths of garnet to show the peak P-T conditions.

0.5–0.6 GPa, and ~540–580°C. Garnet is stable above 420°C, and restricted to pressure ranging from 0.25 GPa to 0.62 GPa. Kyanite-sillimanite transition occurs at a P-T of 510°C and 0.39 GPa. Muscovite-out curve occurs at a range of 610°C–700°C, which is beyond the stability field of the peak equilibrium mineral assemblages. Compositional isopleths of garnet intersect at ~558°C and 0.56 GPa.

The phase diagram for the sample AS-8 was constructed within a P-T window ranging from 0.2 to 0.8 GPa and 300–900°C for the measured bulk composition (Fig. 8b). The topology comprises different stability fields with melt above ~710°C, with fewer hydrous phases. Kyanite-sillimanite transition curve occurs at a temperature above 535°C and pressure above 0.43 GPa. Muscovite-out curve, cordierite-in curve, and melt-in curve occur above 600°C, 630°C, and 710°C respectively. The peak assemblages are garnet-biotite-sillimanite-K-feldspar-cordierite-quartz-melt, followed by prograde assemblages of Garnet-Biotite-muscovite-K-feldspar −plagioclase-kyanite-Quartz and muscovite-biotite-K-feldspar −plagioclase-quartz-rutile as retrograde mineral assemblages. Compositional isopleths for garnet end members intersect at around 790°C and 0.66 GPa in the peak P-T equilibrium condition.

The phase topology for the sample ASK-79 constructed within a P-T window ranging from 0.2 to 0.8 GPa and 300–900°C comprises different stability fields with melt-in curve occurring above ~610°C, with little hydrous phases (Fig. 8c). Kyanite-sillimanite transition curve occurs at a temperature above 575°C and at a pressure above 0.37 GPa. Muscovite-out curve and cordierite-in curve occur at temperatures above 525°C, and 530°C respectively. The peak assemblages are garnet-biotite-sillimanite-feldspar-ilmenite-quartz-melt, followed by prograde assemblages of Muscovite-Biotite-Kyanite-Garnet-Quartz-ilmenite and retrograde mineral assemblages of K-feldspar-muscovite-chlorite-plagioclase-quartz. Compositional isopleths for garnet end members intersect at around 728°C and 0.66 GPa at peak P-T equilibrium condition. The poor convergence of X_{Mn} compositional isopleth may be attributed to the fractionation behavior of garnet because the original rocks contain less than 0.1% 'Mn' and the Mn content falls to negligible at the garnet rims.

4.5.2. T-XH_2O phase diagram

T-aH_2O phase diagrams were constructed to estimate the water content for the samples DL-12, AS-8, and ASK-79 during peak metamorphic conditions (Fig. 9a, 9c, 9e). In sample DL-12, H_2O content was measured for the peak stable mineral assemblages of K-feldspar −plagioclase-garnet-biotite-muscovite-kyanite-rutile-ilmenite-quartz at a fixed pressure of 0.55 GPa and T-window between within 300°C-700°C (Fig. 9a). Intersection of compositional isopleths of garnet and biotite plotted in the phase diagram reveals H_2O content around 0.175 mol%. Similarly, H_2O content was estimated in the samples AS-8 and ASK-79 for the peak stable mineral assemblages of K-feldspar-plagioclase-garnet-cordierite-sillimanite-quartz and K-feldspar-plagioclase-garnet-cordierite-sillimanite-melt-ilmenite-quartz respectively, at a fixed pressure of 0.66 GPa and a T-window between 300°C and 900°C (Fig. 9c, 9e). From the intersection of compositional isopleths of garnet and biotite, actual H_2O content during the peak stage of metamorphism is found to be around 0.05 mol% for AS-8. For the sample ASK-79, an approximated H_2O content of 0.067 mol% was estimated from the intersection of compositional isopleths of garnet and biotite. From the above diagram, it is inferred that the high-H_2O content (>0.1 mol%) in the sample DL-12 is attributed to the major hydrous phases, viz., muscovite, and biotite. At subsequent increase in temperature, hydrous phases like muscovite- and biotite-melting is initiated accounting for a more anhydrous mineral assemblage of K-feldspar-sillimanite in the samples AS-8 and ASK-79, which leads to low-H_2O content (<0.1 mol %). These low value of H_2O during the peak metamorphic conditions suggest dry rocks that further lend support to the attainment of upper amphibolite-granulite facies transition.

4.5.3. Phase diagram based on effective bulk composition

Isochemical phase diagrams were constructed for the samples DL-12, AS-8 and ASK-79 using the EBC data calculated based on the approach of the Rayleigh fractionation principle (Evans, 2004; Gaidies et al., 2006) within the same P-T window as the phase diagram computed by unfractionated bulk composition (Fig. 9b, 9d, 9f). The phase topology of DL-12 (Fig. 9b) comprises peak assemblages of garnet-biotite-K-feldspar-plagioclase-kyanite-quartz-rutile. Sillimanite-kyanite transition curve occurs at a temperature above 530°C and pressure above 0.42 GPa. Compositional isopleths of garnet end members intersect at around 571°C and 0.58 GPa. The phase topology for the sample AS-8 (Fig. 9d) comprises kyanite-sillimanite transition curve above temperature around 535°C and pressure around 0.43 GPa. The cordierite-in curve occurs at a temperature above 500°C, whereas the melt-in curve started to appear above P-T conditions of 0.54 GPa and 765°C. The peak P-T equilibrium conditions of stable mineral assemblages of garnet-K-feldspar-plagioclase-melt-cordierite-sillimanite-quartz-rutile calculated by the intersection of compositional isopleth of garnet end members occur at around 0.64 GPa and 787°C. The phase topology of the sample ASK-79 (Fig. 9f) comprises a kyanite-sillimanite transition curve at P-T conditions above 0.42 GPa and 535°C. Cordierite-in curve started to appear within the P-T range of 0.2 GPa at 355°C to 0.56 GPa at 900°C, whereas melt-in curve appears at a temperature above 745°C and pressure above 0.45 GPa. The sillimanite phase appears in the section at the expense of muscovite. The intersection of compositional isopleth of X_{Fe}, X_{Mg}, X_{Ca}, and X_{Mn} of garnet end members suggests that the peak P-T equilibrium mineral assemblages of garnet-biotite-melt-K-feldspar-plagioclase-sillimanite-quartz-rutile are stable at around 0.69 GPa and 748°C.

4.5.4. Effect of fractionation on phase diagram

For the sample DL-12, the geometry of Garnet-biotite-K-feldspar-plagioclase-kyanite-quartz-rutile stability field for the fractionated bulk compositions is enlarged and shows alteration as compared to unfractionated bulk compositions, while the calculated P-T conditions using compositional isopleths show marginal variations, i.e., from 0.56 GPa and 558°C (unfractionated) to 0.58 GPa and 571°C (fractionated). Muscovite was entirely consumed, whereas plagioclase and rutile appear as new member assemblages in the peak P-T stability field.

For the sample AS-8, the kyanite–sillimanite boundary is slightly displaced towards higher temperature at constant pressure. Muscovite disappears completely from the peak assemblage field and is replaced by sillimanite. Cordierite becomes stable at lower temperatures than in the unfractionated diagram. The melt field is restricted and shifted to higher P–T, whereas the peak assemblage field contracts toward lower P–T, with estimated peak conditions ~30°C and ~0.02 GPa lower than those obtained from the measured bulk composition.

In the sample ASK-79, the peak assemblage field is considerably narrower. The stability of cordierite is displaced to lower P–T and is restricted to pressures ≤0.56 GPa, whereas the kyanite stability field shifts to lower temperature. It is important here to note that the compositional isopleth contour of X_{Fe} from the garnet end member increases toward higher temperature, while X_{Mn} rim isopleths again intersect observed values correctly only in the fractionated model.

Fractionation causes systematic underestimation of both pressure and temperature when using unfractionated (measured) bulk compositions. Across the sample suite, peak conditions derived from measured bulk compositions are typically 3°–20°C and 0.02–0.03 GPa lower compared with EBC-based estimates, because the measured whole-rock composition includes garnet that was no longer part of the reactive system after fractionation. Conversely, EBC modelling yields higher prograde and peak P–T conditions in most samples (except AS-8, where conditions are slightly lower). Garnet compositional isopleths are strongly affected, where X_{Mn} contours shift dramatically, and X_{Fe} values are typically lower (often roughly half) in EBC diagrams. In several cases, the X_{Mn} isopleths for rim compositions intersect the observed

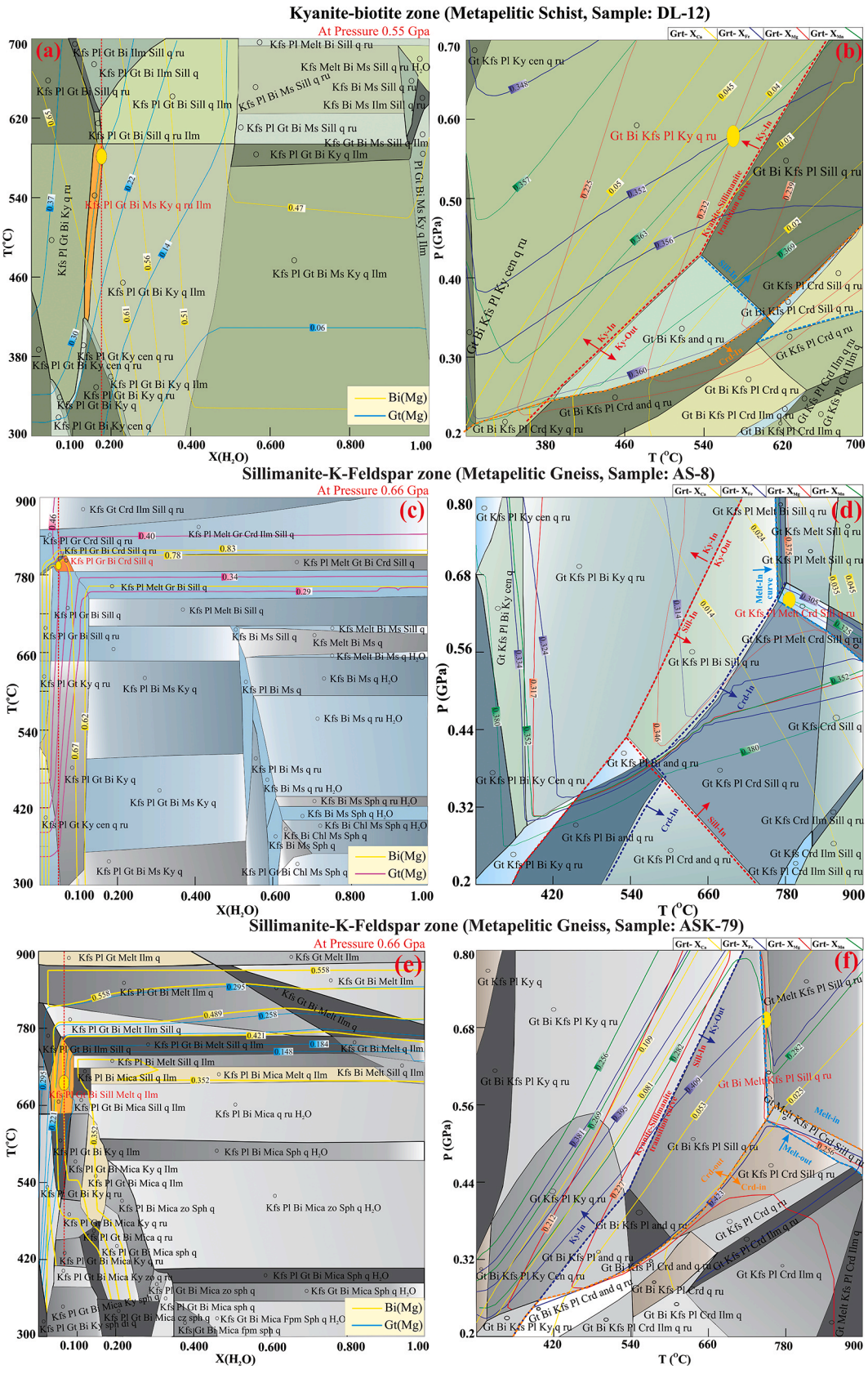

(caption on next page)

Fig. 9. T-XH_2O phase diagram and modified isochemical phase diagram for the kyanite-biotite zone, and sillimanite-k-feldspar zone of the metapelitic schists and gneisses (sample nos. DL-12, AS-8, ASK-79) in the MnNCKFMASHT system. The T-XH_2O phase diagram (in a, c, and e) was constructed using the original bulk compositions derived from the XRF. The modified isochemical phase diagram (in b, d, and f) was constructed using EBC by assuming garnet fractionation during growth. The EBC was calculated using the approaches of Evans, (2004) and Gaidies et al., (2006), based on Rayleigh fractionation principles. The modified bulk compositional data in weight % are: Na_2O 1.71, CaO 1.38, MnO 5.6, K_2O 3.23, FeOT 5.55, MgO 4.17, Al_2O_3 12.02, SiO_2 65.57, H_2O 0.2 TiO_2 0.65; The phase topology has been marked by kyanite-sillimanite transition curve, and cordierite-in curve, and has been contoured and intersected with the isopleths of garnet for the calculation of peak P-T conditions; b. Isochemical phase diagram for the sillimanite-K-feldspar zone of the metapelitic gneisses (sample no. AS-8) in the MnNCKFMASHT system. The modified bulk compositional data in weight % are: Na_2O 3.71, CaO 0.41, MnO 1.30, K_2O 2.46, FeOT 1.29, MgO 1.76, Al_2O_3 10.06, SiO_2 78.87, H_2O 0.1 TiO_2 0.11; The phase topology has been marked by kyanite-sillimanite transition curve, melt-in curve, cordierite-in curve, and muscovite-out curve, and has been contoured and intersected with the isopleths of garnet for the calculation of peak P-T conditions; c. Isochemical phase diagram for the sillimanite-K-feldspar zone of the metapelitic gneisses (sample no. ASK-79) in the MnNCKFMASHT system. The modified bulk compositional data in weight % are: Na_2O 1.69, CaO 3.49, MnO 2.20, K_2O 3.87, FeOT 3.18, MgO 2.08, Al_2O_3 11.71, SiO_2 71.15, H_2O 0.1 TiO_2 0.55; d. The phase topology has been marked by kyanite-sillimanite transition curve, melt-in curve, cordierite-in curve, and muscovite-out curve, and has been contoured and intersected with the isopleths of garnet to show the peak P-T conditions.

values within analytical uncertainty only when fractionation is accounted for. The improvement in precision of P–T estimates is marginal, but the accuracy of retrieved conditions and the match between observed and predicted garnet rim compositions are significantly better when fractionation is taken into account. Caution needs to be exercised as the EBC approach presented here assumes only garnet fractionation and closed-system behavior after segregation. Additional processes such as modification of the effective fluid composition, late diffusional re-equilibration of garnet, or fractionation of other phases like plagioclase, and oxides can further displace phase boundaries and must be evaluated on a case-by-case basis.

As the P-T conditions from the conventional thermobarometric models correspond well with the isopleth thermobarometry and associated peak mineral assemblages on the isochemical phase diagrams, the P-T conditions for the core and rim compositions of the garnet are shown in Petrogenetic Grid System (PGS) of Spear et al., (1999) for the prograde path (Fig. 10). The present P-T path from core to rim is consistent with the observed mineral assemblages and reactions and noticeably different from both the Almora Nappe (Joshi and Tiwari, 2009) and the HHM lying to north of the Main Central Thrust (Hodges and Silverberg, 1988; Spencer et al., 2012) in Kumaun. The calculated P-T is consistent with the muscovite-biotite-quartz-ilmenite ± chlorite (sparse) assemblages in the matrix crystallized during the regressive arm of the regional metamorphism, which is reflected as T_m point.

4.6. Zircon U-Pb ages

The representative CL images and concordia plots for the zircon grains from AS-8 sample are shown in Fig. 11 and Fig. 12. AS-8 is fully representative of the metapelitic gneiss core in the Askot Klippe, based on lithological, structural, and analytical criteria. It comes from the thickest, most leucosome-rich gneiss layer with a peak sillimanite–K-feldspar–cordierite assemblage, and is the only fresh, unaltered exposure located due to limited fresh outcrops in the area. Structurally, it is positioned in the central nappe interior, avoiding greenschist overprint at the margins. Systematic screening showed AS-8 yielded over 140 clean, prismatic zircons suitable for LA-MC-ICPMS, unlike others dominated by detrital or fractured grains, while EPMA on minerals from five samples (including AS-8) gave identical P–T conditions (>780°C, 0.6–0.7 GPa), with matching zircon textures and Th/U ratios. Thus, AS-8 captures the full metamorphic history, making additional samples redundant. Zircons in this sample are transparent, light pink to colorless and predominantly long subhedral to euhedral prismatic crystals. Zircon grains have lengths ranging between 100–200 μm with aspect ratios (length/width) of 3:1–1:1. Most zircons show alternating bands of bright and dark luminescence in CL images displaying core-mantle-rim texture. CL images show relatively bright zircon cores and dark grey mantle and rims. The cores display bright luminescence in CL images, without prominent zoning, and have subrounded outlines, which indicate

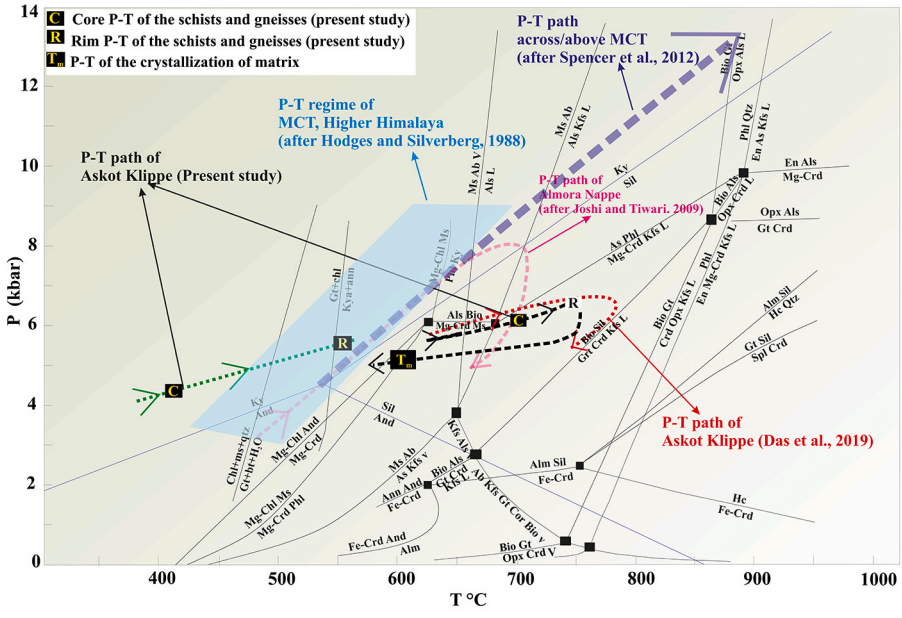

Fig. 10. Simplified petrogenetic grid showing the P-T conditions of core and rim of the selected samples of Almora Group in the system Na_2O-CaO-MnO-K_2O-FeO-MgO-Al_2O_3-SiO_2-H_2O-TiO_2 (MnNCKFMASHT). Petrogenetic grid for metapelitic schists and garnet-cordierite-sillimanite-K-feldspar bearing metapelitic gneisses (modified after Spear et. al., 1999). Comparison of the present P-T data with the available data from other parts of Himalaya.

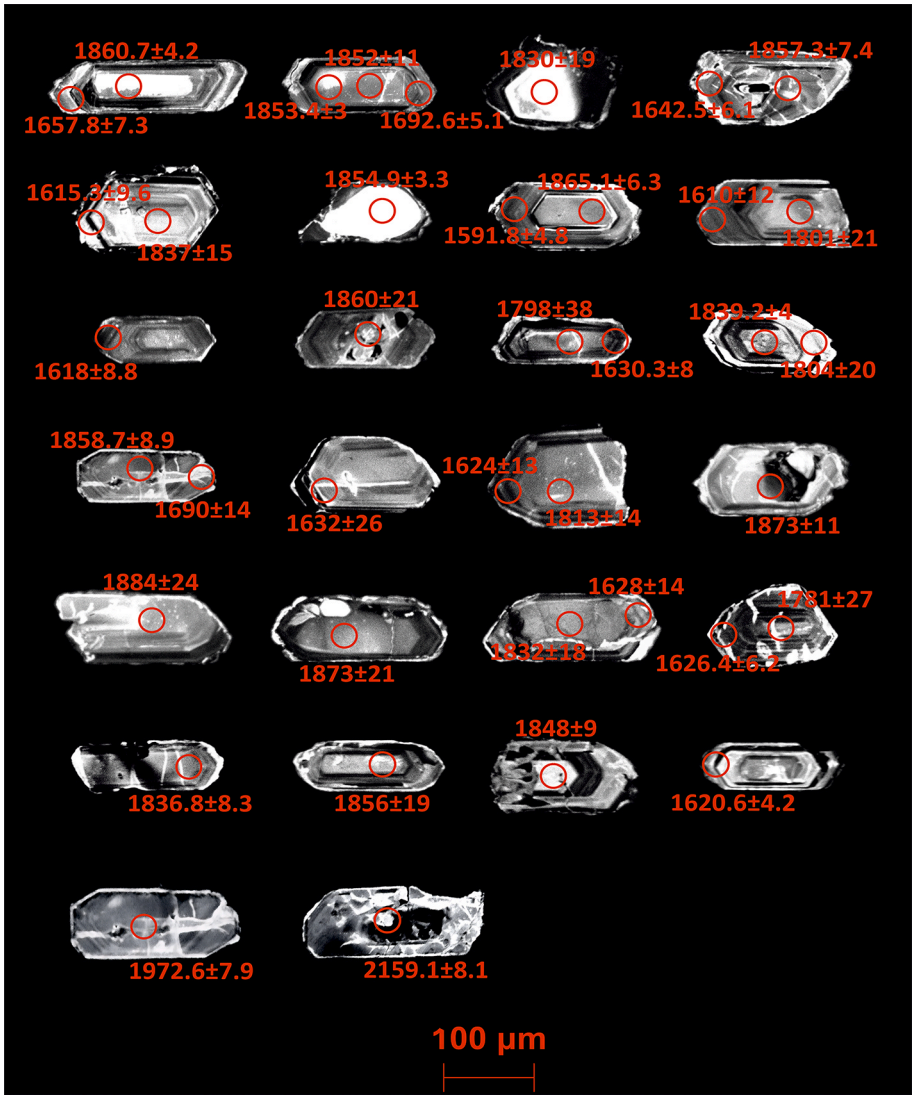

Fig. 11. Representative cathodoluminescence (CL) images of the zircon grains of AS-8 sample from the Askot Klippe, NW Himalaya. The red circles show the position of spots used for LA-MC-ICPMS zircon U-Pb dating. The spot analyses of the core, mantle, and rim of zircon is done to give the detrital and metamorphic ages of the studied sample. Age is represented in "Ma".

resorption or abrasion prior to overgrowth, typical of detrital or inherited magmatic zircons. The lack of zoning suggests homogeneous growth in a melt environment, possibly from Paleoproterozoic granitoids or volcanic arcs along the NICM. Th/U ratios ranging from 0.32 to 0.38 are characteristic of magmatic zircons, where Th is more readily incorporated into the lattice due to its compatibility in igneous melts (Hoskin and Schaltegger, 2003). In contrasts the metamorphic overgrowth on the zircon cores with lower ratios reflects the preservation of primary igneous chemistry despite later overprints. The mantles show moderate luminescence with weak oscillatory to sector zoning. This zoning pattern is suggestive of metamorphic overgrowth, often resulting from solid-state recrystallization or fluid-mediated precipitation during prograde metamorphism. The dominance of mantles in sections suggests significant overgrowth volume. Th/U ratios ranging from 0.1 to 0.3 are typical for metamorphic zircons, where Th is less incorporated perhaps due to competition with other phases or depletion in metamorphic fluids (Rubatto, 2017). The sector zoning further supports metamorphic conditions, as it arises from differential growth rates on crystal faces during slow, diffusion-limited recrystallization. The rims exhibit darker luminescence with an unzoned or homogeneous appearance. This lack of zoning is common in zircons formed during partial melting, where rapid growth in melt pockets homogenizes the structure. The dark CL indicates high U content or radiation damage, aligning with the present evidence of migmatization in the sillimanite-K-feldspar zone. Th/U ratios ranging from 0.02 to 0.09 may be diagnostic of anatectic zircons, as partial melts during high-temperature metamorphism preferentially incorporate U over Th, often due to Th sequestration in accessory phases like monazite (Yakymchuk et al., 2018).

U-Pb dating has been conducted on the core and rim of the same zircon grain. Th, U, and Pb concentrations of the analyzed zircons range from 7.56-821 ppm, 195.3–2701 ppm, and 2.29–307 ppm, respectively; with Th/U ratios of 0.02–0.93 (see Supplementary Table S5). Zircon U-Pb data of this sample defines discordant ages with very few concordant ages, that indicate variable Pb loss. Analyses conducted on the core of the zircons yielded two older ages of ca. 2159.1 ± 8.1 Ma and ca. 1972.6 ± 7.9 Ma respectively. Similarly, spot analyses for mantle of the zircons yielded an upper intercept age of 1850.30 ± 7.63 Ma (Mean square weighted deviation, MSWD, = 2.4, n = 40) while analysis on the rim yielded an upper intercept age of 1616.82 ± 8.41 Ma (MSWD = 3.1, n = 28) which is consistent with the observed peak ages in the relative probability graph of the zircon U-Pb analyses.

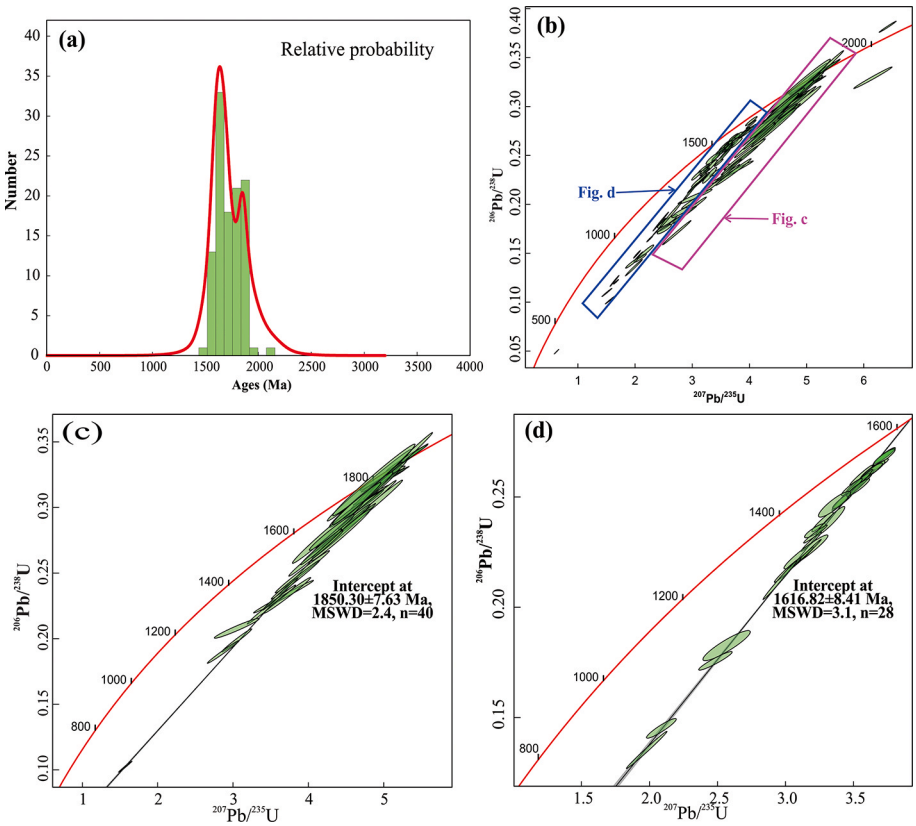

Fig. 12. (a) Relative probability plot and, U-Pb Concordia (b; c: Zircon mantle; d: Zircon rim) of the zircon U-Pb dating (sample: AS-8) from study area, Northwestern Himalaya.

5. Discussions

5.1. Mineral paragenetic evolution

The cross-cutting micas of two generations forming at different angles indicate a continuous change in the orientation of the strain ellipsoid during later metamorphism across all metamorphic zones in the area. The pressure shadow around garnet is developed as a result of synkinematic crystallization of the garnet core and post kinematic crystallization of a relatively inclusion-free rim. The development of scattered tiny garnet idioblasts in the matrix further substantiates that the metamorphism outlasted the deformation. Some garnets show development of fractures due to localized late-stage brittle deformation. In the metapelitic gneisses prograde metamorphism is triggered by the muscovite and biotite dehydration melting reactions, which suggests overstepping the amphibolite facies conditions. It is crucial to mention here that sharp and fresh contacts between the second-generation muscovite-quartz and biotite-quartz indicate the retention of fluid in the rock when it started cooling, a fact corroborated by random orientation of the last-generation coarse muscovite flakes that likely developed by the reaction K-feldspar + sillimanite + melt = muscovite + quartz (Dyck et al., 2020) under plastic conditions induced by the hydrostatic stresses in a melt dominated system. The garnet-biotite-K-feldspar-ilmenite-H_2O phase assemblage likely crossed its stability field as evidenced by the development of incipient reaction rims at the quartz-biotite contact (Caddick et al., 2010) with the garnets showing stronger growth zoning profile from core to rim indicating prograde nature towards higher temperature (see zoning profiles in Fig. 6). Presence of micro-perthites developed due to immiscibility during cooling of the anatectic melts produced at the peak metamorphic conditions that led to formation of the gneisses; corroborate the high temperatures and multiple feldspar phases in the isochemical phase diagram of metapelitic gneisses.

We demonstrate that the metapelitic gneisses in the Askot Klippe are products of in-situ anatexis through a multi-scale, mutually reinforcing dataset; (1) Field-scale continuity through gradational metamorphic progression from greenschist-facies phyllites to kyanite-biotite schists to sillimanite-cordierite gneisses, with concordant foliation and no intrusive contacts (Fig. 3; cf. Searle and Szulc, 2005; Imayama et al., 2019), (2) Petrographic evidence of melting through sillimanite-K-feldspar intergrowths replacing muscovite (Fig. 5d; reaction: Ms + Qtz → Sil + Kfs + H_2O; Spear et al., 1999), (3) Leucocratic segregations with interstitial K-feldspar and quartz (Fig. 3e), interpreted as trapped melt pockets (Sawyer, 1999), (4) Geochemical fingerprint in strongly peraluminous (A/CNK = 1.3–1.6) metapelitic gneisses and biotites with high Al^{vi} (1.8–2.1 apfu), consistent with melt-residue systems (Stevens and Clemens, 1993; Das et al., 2019), (5) P–T constraints through Peak conditions of 6–8 kbar and 735°C–790°C (conventional thermobarometry and phase diagram modeling; fig. 8, fig. 9), within the fluid-absent melting field for metapelites (Spear et al., 1999; White et al., 2001).

5.2. Indiscrepancies between the automated Theriak P-T path and conventional P-T path modelling approach

We compare P-T conditions for the three samples for the modelings using Theriak P-T path and conventional thermobarometry. Admittedly, the two modeling approaches are controlled by the thermodynamic constraints (Spear and Peacock, 1989) and possible sources of error in the system include molar enthalpy and entropy of formation, heat capacity, molar volume, solution models, and Margules parameter (Margules, 1895). It is presumed that the system is closed and there is no exchange of material that could change the compositions and mineral phases present in the rock (Lanari and Engi, 2017). We evaluate the results for the three samples using both the modeling approaches to

verify the data consistency.

The *P-T* paths inferred from the Theriak-Domino MATLAB modeling are not consistent with the textural and mineralogical observations. It is likely that the constraints used in the Theriak P-T path modeling do not correspond with the ambient physical conditions during the metamorphism under question. The probable reasons adversely affecting the reconciliation between the Theriak P-T path modeling and the conventional thermobarometric modeling approach are:

(1) For the sample DL-12, the maximum P-T conditions estimated for metapelitic schists using both conventional geothermobarometry and isochemical phase diagram modelling approach are around 0.55–0.56 GPa and 556-560°C. On the other hand, High-Resolution P-T path modelling approach yields a peak P-T condition ~565°C and 0.59 GPa. As a result, DL-12 shows typical P-T uncertainties of 0.05–0.09 GPa and 5–9°C. High-Resolution P-T path modelling indicates a 5–9°C higher temperature and 0.035–0.04 GPa higher pressure as compared to the other two approaches mentioned earlier. Such slight deviations in P-T estimates using different approaches lie within the uncertainty limits (Palin et al., 2016) for all the studied pelitic schists. Therefore, it can be assumed that the present thermobarometric results from conventional as well as isochemical phase diagram modelling are quite consistent with the High-Resolution P-T path modelling approach.

(2) Using conventional thermobarometry and isochemical phase diagram modelling, AS-8 yields P-T conditions of around 0.65–0.66 GPa and 730-760°C, whereas High-Resolution P-T path modelling approach yields P-T condition ~0.64 GPa and 570°C. The High-Resolution P-T path modelling shows a decrease of 190°C in temperature and 0.02 GPa in pressure. The pressure deviation is negligible, but the temperature deviation is far beyond the uncertainty limits reported by Palin et al. (2016). Similarly, ASK-79 yields P-T conditions of 0.66 GPa and 725°C using conventional as well as isochemical phase diagram modelling, whereas a P-T estimate of around 0.64 GPa and 590°C was retrieved using High-Resolution P-T path modelling approach. There is a P-T deviation of 0.02 GPa and 135°C. Once again, pressure estimates remain insignificant, while the temperature deviation lies outside analytical uncertainty. The magnitude of temperature differences for the metapelitic gneisses are very high compared to the pressure differences because garnet crystallization exceeded temperatures of 600°C which continued up to the peak P-T conditions of metamorphism, supported by its zoning characteristics, diffusional modifications and bulk compositional heterogeneities, which clearly violate the assumptions made by Moynihan and Pattison (2013). The core-rim *P-T* conditions of the metapelitic schist computed by the Theriak P-T path modeling in conjunction with MATLAB correspond well to the *P-T* conditions by the conventional thermobarometric approach. Interestingly, the two approaches yield similar results, which suggest the calculations below 600°C are valid given the limitations of the Theriak P-T path modeling approach. The negligible pressure differences of 0.02–0.03 GPa computed from the above two approaches for the metapelitic schists does not affect the inferred P-T stability fields of peak equilibrium mineral assemblages. The small changes in the calculated pressures likely reflect (very low angle) P-T gradient established for the area rather than meaningful geological variations (Fig. 10).

(3) The *P-T* path modeling using Theriak-Domino software assumes that the garnet must preserve the original chemical zoning with little re-equilibration, implying the temperatures should not exceed 600°C. However, the petrographic study along with the BSE image of garnets in gneisses of the Almora Group shows two distinct generations of garnet growth, one showing the deformed inclusion- rich core while the other shows inclusion-free idioblastic rim, which documents at least two metamorphic phases of (see BSE images and X-ray elemental maps in Fig. 6) garnet crystallization. That the temperature exceeded 600°C is substantiated by the petrography, equilibrium mineral assemblages, thermobarometric estimations, and Perple_X phase section modeling, all of which consistently suggest that the temperatures did far exceed 600°C. The contradiction between the results of the *P-T* path modeling using Theriak-Domino software and the other methods in vogue is expected as the assumptions for the later are not fulfilled for the metapelitic gneisses.

(4) Given the possibility of high-T homogenization inferred by the subdued bell-shaped 'Mn' profile (Woodsworth, 1977), it is likely that the garnet growth continued up to the peak *P-T* conditions. However, the maximum P-T obtained by the Theriak-Domino modeling are 0.63 GPa- 591°C for the garnet rim in the metapelitic gneisses is inconsistent with the generation of K-feldspar-sillimanite assemblage and the attendant melting, which occurs only above 710°C at 0.65 GPa (Dyck et al., 2020) in the pelitic gneisses. Furthermore, the observed zoning data does not correspond to the modeled zoning data of garnet for the samples ASK-79 and AS-8, which highlights the limitations of Theriak P-T path modeling above 600°C.

(5) The effects of resorption and the fractionation behavior of garnet crystal with assumption of fluid saturation in the system play a significant role in shifting the temperature estimation by the Theriak-Domino program.

(6) The most significant difference between the Theriak P-T path modeling and the conventional thermobarometric modeling lies in the observed reaction histories and mineral assemblages of the metapelitic gneisses. Unlike Theriak-Domino program, these are independent of any assumption about the preservation of garnet zoning. Conventional thermobarometric modeling along with the Isochemical phase diagrams are consistent with the observed mineral assemblages and reactions at peak *P-T* equilibrium conditions, like the muscovite-quartz, and biotite-quartz reactions in the rock. Numbers of thermobarometric software programs including THERMOCALC (Powell et al., 1998) and TWQ (Berman 1988, updated 1991; Berman and Aranovich, 1996 for the end-member phases) were used to retrieve the *P-T* for the metapelitic schists and gneisses and they closely correspond to the petrographic observations. However, we demonstrate the Theriak P-T path modeling does not reflect the petrographic observations for metapelitic gneisses of the Askot Klippe.

(7) The temperatures of the studied metapelitic gneisses are the minimum estimates of the peak *P-T* conditions. The development of later assemblages of coarse-grained muscovite-quartz and biotite-quartz, plagioclase, chlorite indicates the water likely did not leave the system and the assemblages crystallized later from the migmatitic melt during the regressive arm of the P-T path while the rocks cooled.

These discrepancies emerge from the assumptions of thermodynamic parameters and mineral compositions. Slight differences in these input parameters and observed mineral assemblages can lead to different results in P-T estimation (Holland and Powell, 1998; Lanari and Engi, 2017). In the present case, observed mineral assemblages, metamorphic reactions and reaction textures play key role in demonstrating the High-Resolution P-T path modelling approach is not applicable to the gneisses in the area and likely not applicable to any gneisses. The garnets in the studied metamorphic rocks crystallized during the prograde metamorphism were subjected to diffusional modification during its re-equilibration as the garnet crystallization temperatures exceeded 600°C, a temperature range that falls outside the applicability of High-Resolution P-T path modelling approach. In addition, Pressure-Temperature (P-T) estimations in metamorphic rocks are subject to

uncertainties from analytical errors, inconsistencies in the properties of internal thermodynamic database (e.g., molar enthalpy of formation, molar entropy, molar volume, heat capacity, bulk modulus, Landau parameters, and Margules parameters; White et al., 2014), and closed-system behavior of garnet. Detailed analyses of garnet fractionation at each step of its crystallization, equilibrium kinetics, reaction mechanisms, and the relationship between initial Bulk composition and effective Bulk composition of the garnet (Tinkham and Ghent, 2005) may be useful to better constrain the thermal evolution of these metamorphic rocks.

The petrographic observations clearly show disequilibria between the muscovite-quartz, plagioclase-quartz, muscovite-plagioclase, biotite-quartz, and biotite-garnet indicated by corroded boundaries while the K-feldspar-sillimanite and K-feldspar-cordierite contacts show sharp boundaries that suggest equilibrium. The garnet chemical profile for the metapelitic schists and gneisses reflects the *P-T* conditions during the garnet growth. During the waning stages of metamorphism when the rock was being returned to shallower crustal levels along the retrogressive arm of the *P-T* loop, the stable coarse muscovite and biotite flakes along with the quartz grains with sharp boundaries crystallized at 571°C temperature and 0.53 GPa pressure.

While the automated high-resolution P-T path modeling using Theriak-Domino in conjunction with MATLAB serves as a powerful tool for reconstructing prograde metamorphic trajectories from preserved compositional zoning in garnet crystals, it is inapplicable to high-temperature environments, particularly for melt-bearing metapelites, where evidence of partial melting suggests supra-solidus conditions. The model's foundational assumptions limit its applicability beyond the wet solidus, which means the modeling cannot account for melt production or its effects on effective bulk composition, often resulting in underestimated peak temperatures that align more closely with lower amphibolite facies rather than the granulite transition facies suggested by textural evidence and conventional methods for the present area. Furthermore, at elevated temperatures, garnet zoning preservation breaks down due to diffusion-driven homogenization, which can modify compositional profiles and affects the accuracy of isopleth intersections used in the modeling. However, kinetic considerations, such as diffusion modeling employing finite difference methods accounting for Fe-Mg-Mn-Ca diffusivities may be integrated to test sensitivity to bulk composition adjustments for melt loss, which can help constrain the timescale and thermal evolution of the rock Given the consistent discrepancies where the Theriak yields lower temperatures compared to the conventional thermobarometry and phase diagram modeling in supra-solidus regimes, it is of limited applicability, and its results should not be overemphasized.

5.3. Geochronological evidence

In the present sample AS-8, it is imperative to note that zircon cores having high luminescence, unzoned, and homogeneous structures preserve the initial growth during peak anatexis (Kohn, 2017). The zircon core in these conditions might have formed by partial melting followed by dissolution and reprecipitation (Rubatto, 2017). Although, Th/U ratio in the core of zircon grains falls above 0.1 indicating magmatic precursor, the evidence of high Th/U ratio (>0.1) for early-formed metamorphic zircon near peak conditions due to the inclusion of Th during high-temperature anatexis (Yakymchuk et al., 2018) cannot be ruled out. Moreover, the majority of workers believe that high Th/U values in the core of zircon suggest *syn*-metamorphic, high-T anatectic origin (Schaltegger et al., 1999; Harley et al., 2001; Hokada and Harley, 2004), which corroborates well with the present arguments. On the other hand, weak to strong oscillatory zoning observed in the mantle and rims of zircon crystals indicate metamorphic origin, particularly where fluid-influenced thermal conditions prevail during partial melting (Schaltegger et al., 1999; Corfu et al., 2003). Further, low Th/U ratios (<0.1) in the rim of zircon crystals due to possible 'U' enrichment during recrystallization (Harley et al., 2007) and observed oscillatory zoning resulting from kinetic feedback at the crystal-melt interface driven by the anatectic melts (Yardley et al., 1991) are the key indicator of metamorphic growth of zircon.

The multiple metamorphic origin of zircon was further ratified by the petrographic evidences, viz., (1) two generations of mica, (2) two generations of garnet with earlier cores preserving prograde conditions and later overgrowths recording a secondary event, (3) Cordierite in the rims of garnet suggesting a late-stage decompression, aligning with the younger zircon rims (Harris and Holland, 1984).

The unzoned zircon cores are interpreted as detrital based on their high Th/U ratios (>0.10) and Archean to Paleoproterozoic ages (2159 Ma and ca. 1972 Ma). The age of ca. 1860–1884 Ma can be considered as the first anatectic event to have preserved the initial growth during peak anatexis, often coeval with Sillimanite and K-feldspar replacing muscovite, whereas the age of ca.1610–1616 Ma can be attributed to be the second anatectic event and the age of peak metamorphism, exhibited by the mineral assemblages of garnet-K-feldspar-sillimanite and coeval with Cordierite grains around garnet rim. Moreover, zircon U–Pb systematics shows no Pb-loss or young rims in these nappe-core samples (concordance ≥95%), confirming closed-system behavior since ~1610 Ma. Therefore, the present data suggest that garnet-sillimanite-K-feldspar bearing metapelitic gneisses from the Askot Klippe like other klippen of Lesser Himalaya preserve pre-Himalayan metamorphic signatures and maintained the same metamorphic grade through subsequent geological processes up to Himalayan orogenesis, without recording any overprint of Himalayan metamorphism due to limited Cenozoic reworking (Mukherjee et al., 2024, Joshi et al., 2025). These equilibrium conditions in garnet-sillimanite-K-feldspar mineral assemblages persist because these rocks are possibly derived from the stable cratonic interiors, and least affected by the subsequent later deformation and metamorphism since Paleoproterozoic, thus avoiding deep burial or fluid influx during the Himalayan cycle (Kohn, 2014). In this backdrop, we can conclude that the 1860–1884 Ma and 1610–1616 Ma ages reflect two Paleoproterozoic metamorphic events, supported by texturally and chemically controlled zircon domains (core-mantle-rim), diagnostic melting reactions, and the inferred metamorphic ages, particularly ~1610–1616 Ma event, are consistent with peak P-T conditions independently obtained from EBC phase diagram modeling, providing a robust cross-validation between zircon U–Pb chronology and the metamorphic framework.

5.4. Implications for regional geodynamics

Based on the whole-rock geochemistry, High-Resolution P-T path modeling, thermobarometric data as well as isochemical phase diagrams, we show that the highest-grade metamorphic rocks of the Almora Group of the Askot Klippe belong to amphibolite-granulite facies conditions that exceeded 0.65 GPa and 745°C. Later during cooling, while they returned to shallower levels with essentially no fluid loss, the rocks witnessed solidification of the migmatitic melt with crystallization of micas involved in the stable muscovite-quartz, biotite-quartz and muscovite-plagioclase assemblages. The melting/anatexis marks the highest metamorphic grade in the central parts of the klippe. There are marked similarities in the lithotectonic setup, and textural-mineralogical relations, viz. the occurrence of garnet porphyroblasts with synkinematic cores and inclusion-free idioblastic rims, and structural details like the occurrence of the highest-grade assemblages in the antiformal cores of the Almora Group, between the Askot Klippe and the Almora Nappe.

P-T path reported in the present study corresponds well with the *P-T* path reported by Das et al., (2019) for the Askot Klippe. It is interesting to note that the P-T paths for the prograde arm of the Almora Nappe (Joshi and Tiwari, 2009) and the prograde arm deduced for the High Himalayan Metamorphics (HHM) (Hodges and Silverberg, 1988; Spencer et al., 2012) correspond well, which favours the correlation of

the HHM and the Almora Nappe metamorphics.

The shallow P-T paths deduced for the Paleoproterozoic metamorphism in the present work and Joshi et al. (2025) suggest low angle subduction, which has been suggested as the most common subduction type for orogenies older than 1.6 Ga (Abbott et al., 1994; Smithies et al., 2003; Cawood et al., 2006; Hawkesworth et al., 2016; Perchuk et al, 2023, 2025). This substantiates our inference that the spatiotemporal setting of Paleoproterozoic metamorphism in the Askot Klippe in Lesser Himalaya is distinct from the P-T trajectory deduced for the Almora Nappe (Joshi and Tiwari, 2007; 2009) and the High Himalayan Sequences (Hodges and Silverberg, 1988; Spencer et al., 2012). A schematic representation of the tectonic set up of the Kumaun Himalaya (Fig. 13) for the crustal shortening induced thrusting during the Cenozoic Himalayan orogeny (modified after Celerier et al., 2009a and Das et al., 2019), depicts the mechanism of the southward tectonic emplacement of the Lesser Himalayan klippen (Askot and Chhiplakot) and the Almora Nappe, with the tectonically underlying granite-granodiorite equivalents of Ramgarh Group as the basement.

5.5. *Formation of the Columbia supercontinent and its close association with the Lesser Himalaya*

The Columbia supercontinent initially amalgamated during 2.1–1.8 Ga with the close packing of several major cratonic fragments of the world, namely America, Africa, Australia, Antarctica, Siberia, Laurentia, Baltica, Scotland, Greenland, and India (Fig. 14a), including the North Indian Cratonic Block (NICB) and South Indian Cratonic Block (SICB) along the Central Indian Tectonic Zone (CITZ) (Yedekar et al., 1990; Jain et al., 1991; Mazumder et al., 2000; Rogers, 2000; Rogers and Santosh, 2002; Zhao et al., 2002; Condie, 2002). This assembly occurred in two stages: Stage I (~2.0–1.8 Ga) involving initial accretion through subduction and continent–continent collisions, forming the mega-continent Columbia with global Paleoproterozoic mobile belts like the Trans-Hudson and Nagssugtoqidian orogens, and Stage II (~1.8–1.6 Ga) characterized by extensional rearrangements and subordinate collisions, as evidenced by metamorphic records showing a turnover from low- to high-temperature/pressure conditions globally (Volante and Kirscher, 2024; Brown et al., 2024). The present data suggest robust linkages between the NICM—the northernmost extension of the Aravalli-Delhi Mobile Belt (ADMB) of the NICB—and the North China Craton (NCC), indicative of these terrains of South Asia being contiguous during the Columbia Supercontinent assembly. Specifically, a metamorphic age of 1.85 Ga from the Trans-North China Orogen is consistent with the present geochronological data from the Lesser Himalayan metamorphic rocks, which may strongly represent juxtaposition of the NICM with the North China Craton during Columbia assembly (Kusky et al., 2016; Wu et al., 2018; Wu et al., 2022). This correlation is bolstered by paleomagnetic and detrital zircon provenance studies that place the NCC adjacent to the northern margin of the ICB during the late Paleoproterozoic, with shared subduction-accretion signatures preserved in ophiolitic mélanges and arc-related granitoids dated at ~1.9–1.85 Ga along the NCC's southern margin (Kusky et al., 2007; Wu et al., 2018). Further, seismic imaging reveals thick slab debris in the mantle beneath the NCC, supporting double-sided subduction models that facilitated rapid amalgamation, with the Central Orogenic Belt forming at ~1.85 Ga through collision of the Western and Eastern Blocks (Santosh, 2010; Zhang et al., 2012). The present 1.62 Ga metamorphic event is consistent with protracted outgrowth along continental margins after the main ~1.8 Ga welding of Columbia's core, extending amalgamation processes to at least ~1.6 Ga in peripheral regions (Zhao et al., 2004; Kirscher et al., 2021; Volante et al., 2022). Geochronological data from U-Pb zircon dating in the metapelitic gneisses may represent a collisional tectonic setting, potentially linking the NICM to the Eastern Cathaysia Block, as proposed in reconstructions where the Lesser Himalaya connects to the South Korean Peninsula (Yu et al., 2012; Wang et al., 2021). This late accretion is consistent with active margin dynamics on the Indian Block, evidenced by similar ~1.6 Ga events in adjacent terranes of Cathaysia Block, reflecting ongoing subduction-accretion rather than craton-wide stability (Kaur et al., 2021; Xia and Xu, 2019).

The lack of a comparable ~1.62 Ga metamorphic event in the NCC can be attributed to its earlier stabilization following the ~1.85 Ga Trans-North China Orogen collision, which concluded the craton's assembly (Zhao et al., 2002; Kusky et al., 2007). Post-1.85 Ga, the NCC transitioned to an extensional regime with rifting and anorogenic magmatism from ~1.8–1.6 Ga, marking the onset of Columbia's fragmentation rather than active collision (Lu et al., 2008). This intraplate setting precluded major collisional metamorphism at ~1.62 Ga in the NCC's core, while peripheral margins like the NICM experienced ongoing tectonic activity due to differing block juxtapositions, viz., the ICB's linkage to Cathaysia rather than direct adjacency to the NCC in some previous models (Johansson, 2009; Yu et al., 2012). Paleomagnetic and geological data further suggest that by ~1.6 Ga, the NCC was undergoing rifting along its northern margin, separating from other cratonic blocks without high-grade metamorphic overprint (Zhang et al., 2012). Evidences lean towards spatial heterogeneity in Columbia's assembly, where the NICM-Cathaysia Block connection might have experienced protracted collisional outgrowth, while the NCC, potentially more internal or adjacent but not directly involved in this margin,

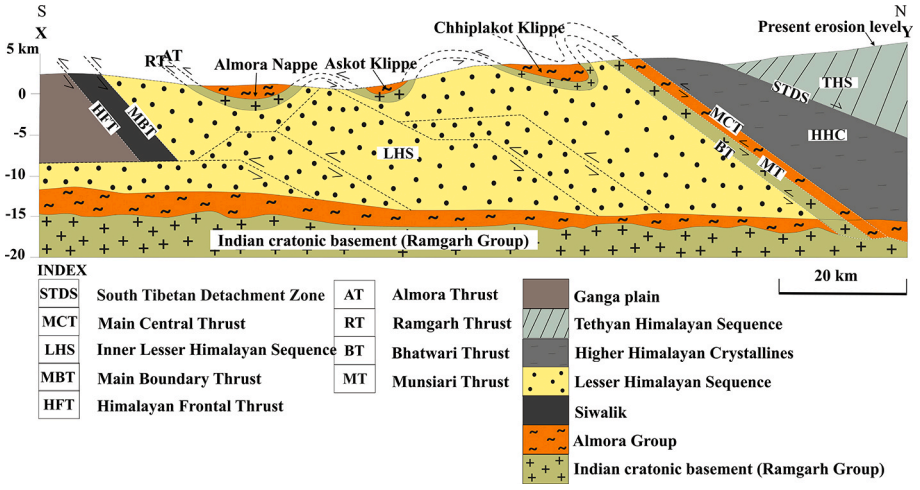

Fig. 13. Simplified cross section of the Kumaun Himalaya depicting the Askot Klippe along with the Almora Nappe in the Kumaun Lesser Himalaya (modified after Celerier et al., 2009; Das et al., 2019). The root zone of the thrust sheet is also shown in the High Himalaya. The P-T paths of the Askot Klippe, Almora Nappe and MCT of High Himalaya are shown to demonstrate the strength of correlation between the nappes and klippen of NW Kumaun Himalaya.

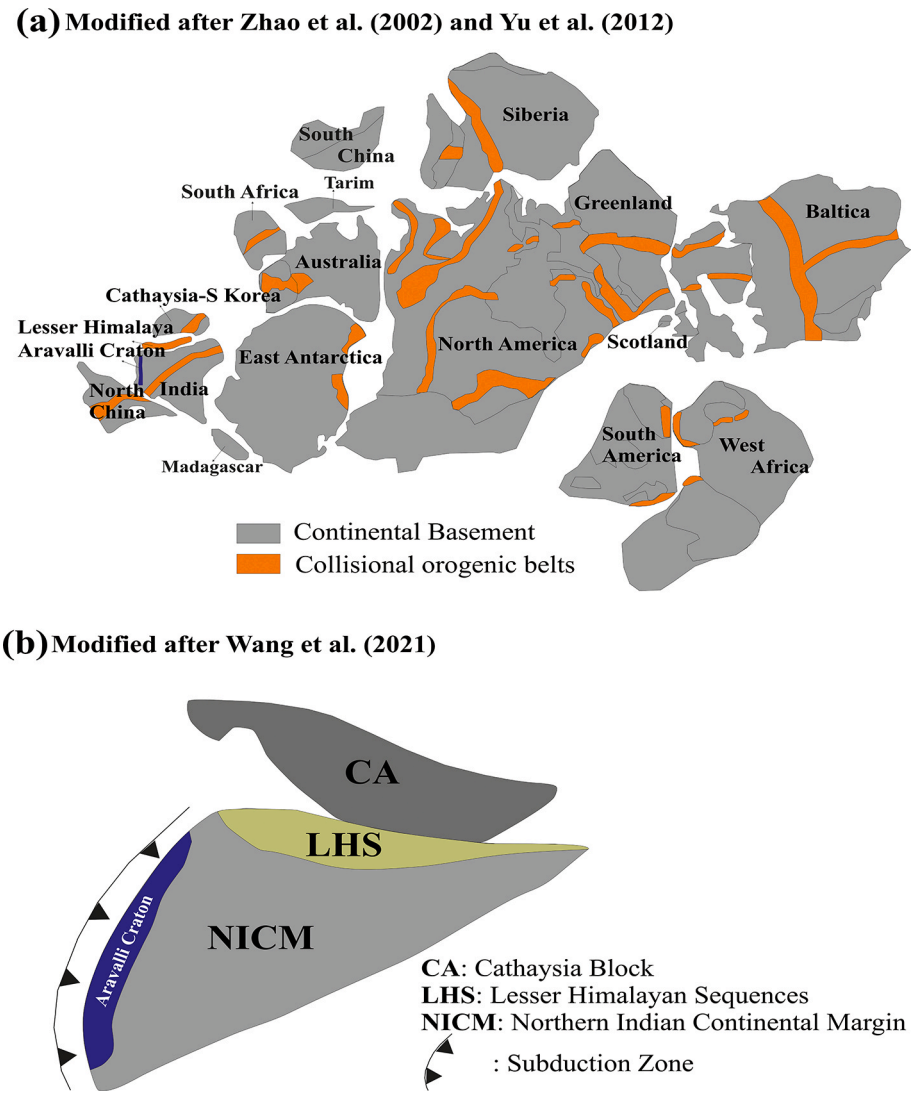

Fig. 14. Paleogeographic and paleotectonic configurations of Columbia Supercontinent (Modified after Zhao et al. 2002; Yu et al. 2012; Wang et al. 2021).

underwent post-collisional extension. This ~1.8–1.6 Ga "magmatic quiescence" in the NCC, with episodic extension, contrasts sharply with the collisional metamorphism in the Askot Klippe.

Magmatic linkages among the ADMB of the NICB, NW Himalaya, and Cathaysia Block, along with relations based on granulite facies metamorphism between the NICB and Cathaysia, were previously established (Yu et al., 2012; Wang et al., 2021), suggesting the NICM was adjacent to the Cathaysia Block (CB) along the Lesser Himalayan Sequences (Fig. 14b). These linkages are strengthened by detrital U-Pb zircon ages from Lesser Himalayan Crystalline Sequence (LHCS) metasedimentary rocks yielding maximum depositional ages of ca. 1.85 Ga, matching those in the Aravalli region and Eastern Cathaysia Block, indicating synchronous arc magmatism and subduction (Mandal et al., 2016; Mukherjee et al., 2019). The present data on high-grade Paleoproterozoic metapelitic gneisses in the NW Himalaya further bridges the gap between the NICB and CB by reporting amphibolite-granulite facies transition rocks from the NICM exposed in the NW Himalaya. These rocks exhibit isotopic similarities in 'Hf' and 'O' compositions, reflecting reworking of Neoarchean–Paleoproterozoic crust in a convergent setting, akin to those in the Eastern Cathaysia Block and South Korean Peninsula (Yu et al., 2012; Cawood et al., 2020). In the Himachal Himalaya, U-Pb zircon ages of ~1.85 Ga from granitic gneisses like the Wangtu and Baragaon represent protolith crystallization in an arc setting, with trace elements showing continental crust remelting and negative anomalies in Ta, Nb, P, Ti (Miller et al., 2000; Webb et al., 2011).

There are multiple lines of evidence for the breakup of different continental cratonic blocks (Bleeker, 2003) and their globally well documented irregular, non-episodic amalgamation, dissemination, and re-amalgamation in the form of supercontinents from the Paleoproterozoic to Phanerozoic (Zhao et al., 2002, 2004; Ernst et al., 2013).

Here we present the hitherto missing evidence of pre-Himalayan polymetamorphic events during the Columbia configuration, including the ~1.85 Ga event tied to peak collision and the ~1.62 Ga event marking post-collisional rifting, as seen in Ultra High-Pressure Metamorphism (UHPM) in Eastern Ghats (~1.6 Ga) and intrusions of the Salari Granite (~1.54 Ga) (Yin et al., 2010; Bhowmik et al., 2012). To substantiate our arguments, we propose a model (Fig. 15) to demonstrate the tectono-metamorphic evolution of the metapelitic rocks of the Askot Klippe and suggest their paleo-architectural association with the Aravalli Supergroup and the Cathaysia Block during the Columbia configuration. This model incorporates a three-stage divergent double-sided subduction: Neoarchean subduction beneath Eastern Cathaysia, ~1.95 Ga double subduction with slab rollback forming LHCS magmatic belts, and ~1.9–1.8 Ga soft collision producing *syn*-collisional granites and back-arc rifting (Ahmad et al., 1999; Kohn et al., 2010; Kaur et al., 2013).

The Aravalli-Delhi Mobile Belt (ADMB) of NW India comprises

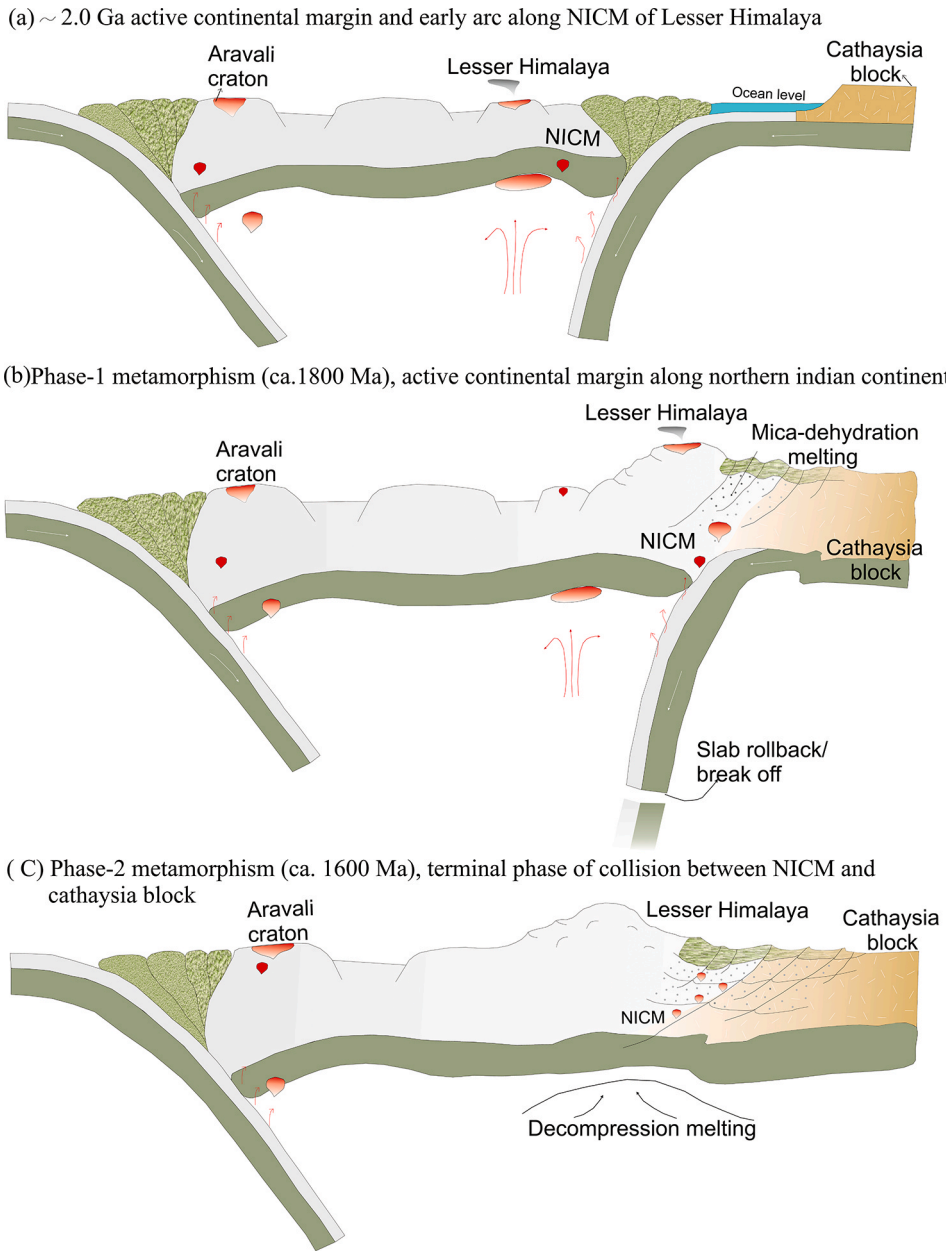

Fig. 15. Model depicting tectonometamorphic evolution of the Paleoproterozoic Lesser Himalayan metapelitic gneisses during Columbia assembly. (a) represents an early arc scenario along NICM and extension of Aravalli Craton and Cathaysia Block into the Lesser Himalayan Sequences; (b) represents subduction scenario facilitated by slab roll-back and attendant mica dehydration melting giving rise to garnet-K-feldspar-cordierite bearing metapelitic gneisses; (c) represents probably the final phase of collisional event between NICM and Cathaysia Block.

Archean and Paleoproterozoic metamorphic rocks (Joshi, 1984; Sharma et al., 1987; Joshi et al., 1993; Sinha et al., 1998) which extends up to NW Himalaya to comprise NICM (Meert and Pandit, 2015). The granulite facies metamorphism in the 'Sand Mata' area of ADMB has been dated at 1.90–1.78 Ga using zircon-monazite ages by Ghosh et al., (2023), which also falls in the age bracket for the two phases of metamorphisms within the Askot Klippe, aligning with global intermediate- to high-T/P metamorphic peaks during Columbia's Stage I (Brown et al., 2024). Paleoproterozoic magmatism, metamorphism, isotopic signatures in Aravalli Supergroup and Lesser Himalaya and granitic intrusions in the Cathaysia Block suggest these three supracrustal blocks were involved in an Andean-type tectono-magmatic arc-subduction set-up (Yu et al., 2012; Kaur et al., 2013; Wang et al., 2017; Zhao et al., 2023) and culminated in an intra-cratonic Paleoproterozoic collisional orogeny during the Columbia assembly. Shared detrital zircon peaks at ~2.5 Ga and ~1.88 Ga between Aravalli/Delhi Supergroups and Lesser Himalayan formations match the ~1.9 Ga Badu Complex in Cathaysia, with synchronous ~1.88–1.86 Ga granulite metamorphism (Richards et al., 2005; Cawood et al., 2018).

The NICM witnessed collisional orogenic activities, subduction, accretion, and volcanic arc trench interplay based on the recent work on the per-aluminous Paleoproterozoic granitic gneisses of the Ramgarh Group of Kumaun Himalaya (Das et al., 2019, Patel et al. 2025) and S-type granites of Lesser Himalayan rocks (Kohn et al., 2010), which is in keeping with the model of Columbia configuration by Hou et al. (2008). Our data suggest that the metapelites of the Askot Klippe underwent at least two distinct Paleoproterozoic metamorphic events, with the first metamorphic event at ca. 1.85 Ga and the second one and the attendant crustal anatexis at ca. 1.62 Ga. We relate the ca. 1.85 Ga and ca 1.62 Ga dates during the Columbia amalgamation, with the former tied to

subduction-collision (e.g., HP granulite at ~1.87 Ga in related orogens) and the latter to extensional phases with mafic magmatism (~1.69–1.66 Ga) (Brown et al., 2024). The ca. 1.62 Ga event may represent the last collisional tectonothermal event recorded from any of the Precambrian Lesser Himalayan rocks associated with subduction-accretion processes, and these are comparable to the youngest dates recorded for the Columbia assembly in Australia (Volante et al., 2020; Volante and Kirscher, 2024), including Barrovian-type intermediate-T/P metamorphism from ~1.65–1.60 Ga collisions (Cawood et al., 2020). Some of the detrital zircon cores from the area yielded older dates ranging between ca. 2.16 Ga, and ca.1.97 Ga, suggesting that the pelitic precursors of the *syn*-Collisional metapelitic gneisses of Askot Klippe (Das et al., 2019) were deposited in the proto-ocean basins within the NICM. The provenance of these sediments was likely located in the Indian shield which acted as a source for sediments rich in Al_2O_3 and K_2O, with detrital populations matching those in the inner Lesser Himalaya (2.05–1.80 Ga zircons) (Spencer et al., 2017).

Yu et al. (2012) compared the Cathaysia Block which has metamorphic ages of ca. 1.89–1.83 Ga, with other Paleoproterozoic orogens globally and found that it has marked similarities with the South Korean Peninsula and the Lesser Himalaya of NW India. They conclude that the eastern Cathaysia block and the South Korean Massif were closely linked to the Lesser Himalayan rocks during the Paleoproterozoic assembly of the Columbia supercontinent, supported by Paleoproterozoic magmatism in Cathaysia tracing its position adjacent to India (Xia and Xu, 2019). Our metamorphic dates of ~1.85 Ga for the pelitic gneisses from the Askot Klippe fall between 1.89–1.83 Ga dates suggested for the Paleoproterozoic orogeny in the Wuyishan terrane of the Cathaysia Block (Li and Zhao, 2007; Xiang et al., 2008; Yu et al., 2009). The Paleoproterozoic orogeny in the Cathaysia Block has been linked to the Columbia Supercontinent assembly (Rogers and Santosh, 2002; Zhao et al., 2002). Auden (1935); Valdiya (1980); and Bhargava (2000) argued for the possible extension of Aravalli into the Kumaun Lesser Himalaya, which is supported by the present work. Our results also suggest further extension of these rocks into northeast China.

The metamorphic history in the Askot Klippe shows striking similarities to those of the Paleoproterozoic high-grade terranes in adjacent regions. The present event of ca. ~1.85 Ga aligns well with granulite-facies metamorphism in the Badu Complex of the Cathaysia Block, where zircon records collisional orogeny at 1.89–1.88 Ga under similar P-T conditions driven by arc-continent collision (Yu et al., 2012). Likewise, the Aravalli Basin in NW India experienced amphibolite to granulite facies transition at ca. ~1.9–1.8 Ga, with prograde paths involving biotite-garnet-kyanite assemblages evolving to sillimanite-K-feldspar-cordierite, mirroring the reaction textures and P-T trajectories observed in our study (Wang et al., 2019). In the Vindhyan Basin, north-central India, metamorphic overprints at ~1.8–1.6 Ga reflect comparable crustal thickening and heating, with evidence of fluid-assisted anatexis similar to the present study (Zhang et al., 2025). These comparisons underscore a unified metamorphic framework, where early greenschist-amphibolite conditions (ca. 1.85 Ga) represent initial subduction, evolving to granulite-grade peaks (ca. 1.6 Ga) during final collision, consistent with Columbia's peripheral orogens (Wang et al., 2018). Basin development in the Lesser Himalaya during the Paleoproterozoic involved sedimentation in arc-related basins, transitioning to collisional forelands amidst supercontinent assembly. This transformation parallels the Aravalli Basin's evolution from a passive margin at ca. ~2.2 Ga with rifting to an active margin with arc magmatism and closure by ~1.8 Ga, facilitated by subduction rollback and accretion (Wang et al., 2019). In the Cathaysia Block, the Badu Complex protoliths were deposited in proximal arc basins synchronous with ~2.5 Ga volcanism, followed by ~1.9 Ga basin inversion during orogeny (Yu et al., 2012). The Vindhyan Basin exhibits analogous shifts, with early rift basins (~1.8 Ga) giving way to foreland settings by ~1.6 Ga, reflecting tectonic responses to Columbia assembly and initial rifting (Zhang et al., 2025). These evolutions highlight episodic orogenic extension-compression cycles, with the Lesser Himalaya's nappes and klippen preserving inverted basin remnants linked to the extension of the ADMB and docking of Cathaysia Block (Wang et al., 2018). Provenance analyses reveal shared source terrains across these regions. In the Aravalli Basin, sedimentary provenance shifts from local Archean cratons (~3.3–2.5 Ga) to Paleoproterozoic arcs (~1.9–1.8 Ga), with Hf-O isotopes suggesting episodic reworking of juvenile material during Columbia assembly (Wang et al., 2018; Wang et al., 2019). The Vindhyan Basin records similar provenance variations, in which early sequences are dominated by ~2.5–1.9 Ga zircons from northern Indian arcs and later one transition to ~1.6 Ga inputs from collisional orogens. This progression implies sediment supply from ADMB and potentially Cathaysia-linked terranes (Zhang et al., 2025). These overlaps support paleogeographic proximity, with sediment routing from arc systems along the NICM to basins in Lesser Himalaya, ADMB, and Cathaysia during Columbia's outgrowth.

In the backdrop, the metapelitic gneisses of Askot Klippe are likely reworked northernmost extension of the cratonic rocks of the Aravalli Delhi Mobile Belt, which hold significant clues for the Paleoproterozoic reconstructions during Columbia Supercontinent assembly, because of the coeval relationship among the LHCS and Eastern Cathaysia Block (Webb et al., 2011; DeCelles et al., 2000; Gehrels et al., 2011).

6. Conclusions

Our study in the Askot Klippe of NW Lesser Himalaya uncovers a polymetamorphic history linked to the late-stage assembly of the Columbia supercontinent. Through integrated petrographic analysis, whole-rock geochemistry, thermobarometric calculations, phase diagram modeling, and U-Pb zircon geochronology, we identify multiple metamorphic events: an initial ca. 1.85 Ga episode reaching at least upper greenschist facies conditions in an accretionary wedge along the convergent NICM-Cathaysia margin, and a subsequent ca. 1.62 Ga event reaching amphibolite-to-granulite facies, driven by subduction-accretion, slab rollback, and associated crustal anatexis. Notably, high-resolution P-T path modeling proved unreliable for these polymetamorphic gneisses, yielding inconsistencies with other methods, stemming likely from other kinetic factors such as garnet resorption, EBC changes from fractionation, anatectic melt presence, and non-fluid-saturated equilibrium conditions. The derived P-T paths diverge both from those in the High Himalayan Metamorphics (HHM) and Almora Nappe, suggesting distinct tectonic regimes. This extended subduction phase may be consistent temporally with the 1.7–1.6 Ga Mazatzal and Labradorian orogenies, representing Columbia's final marginal outgrowth along the NICM prior to rifting. On a regional scale, these findings further lend support to the tectonic connections among the Aravalli-Delhi Mobile Belt, the NICM, and the eastern Cathaysia Block, underscoring their roles as key Paleoproterozoic elements in Columbia's assembly.

CRediT authorship contribution statement

Mallickarjun Joshi: Writing – review & editing, Visualization, Validation, Supervision, Investigation, Funding acquisition, Formal analysis, Conceptualization. **Biraja P. Das:** Writing – review & editing, Writing – original draft, Visualization, Validation, Methodology, Investigation, Funding acquisition, Formal analysis, Data curation, Conceptualization. **Shubham Patel:** Writing – review & editing, Visualization, Methodology, Investigation, Funding acquisition, Formal analysis, Data curation. **Daniel Pastor-Galán:** Writing – review & editing, Visualization, Supervision, Investigation. **Naresh C. Pant:** Writing – review & editing, Visualization, Supervision, Conceptualization. **A. Krishnakanta Singh:** Writing – review & editing, Visualization, Validation. **Govind Oinam:** Writing – review & editing, Visualization, Formal analysis. **Alok Kumar:** Writing – review & editing, Visualization, Validation. **Ankit Kumar:** Writing – review & editing.

Funding

The present work is funded by the University Grants Commission (UGC), India and MoES/P.O. (Geo)/101(a)/2017, Government of India.

Declaration of competing interest

The authors declare the following financial interests/personal relationships which may be considered as potential competing interests: Dr. Biraja P. Das reports financial support was provided by University Grants Commission. If there are other authors, they declare that they have no known competing financial interests or personal relationships that could have appeared to influence the work reported in this paper.

Acknowledgements

As these ideas developed over a long time MJ acknowledges the financial support under a project from Ministry of Earth Sciences, Government of India, financial grants by the Department of Science and Technology, Government of India, CAS-I and II grants by the UGC, New Delhi, to the Department of Geology, Banaras Hindu University and the Head, Department of Geology for providing necessary facilities for the work. BPD acknowledges Dr. D.S. Kothari fellowship cell, UGC (BSR) for providing the financial support to carry out the research work. AK and SP acknowledge the RJP-PDF IOE grant Dev (6031). Prof. NVC Rao and Dr. Dinesh Pandit are thanked for providing the EPMA facility at Dept. of Geology, Banaras Hindu University. MJ gratefully acknowledges Prof. Ram S. Sharma, late Prof. K. S. Valdiya, Prof. O.N. Bhargava, and Prof. A. K. Jain for constructive discussions at various stages of the work. MJ acknowledges Prof. James Connolly for his fruitful suggestion on the manuscript. MJ thanks the Director and scientists of the Wadia Institute of Himalayan Geology, Dehradun, for providing the whole rock XRF analyses.

Appendix A. Supplementary data

Supplementary data to this article can be found online at https://doi.org/10.1016/j.precamres.2026.108038.

Data availability

Data will be made available on request.

References

Abbott, D., Drury, R., Smith, W.H.F., 1994. Flat to steep transition in subduction style. Geology 22, 937–940.
Ahmad, T., Kaulina, T.V., Mishra, A., 1999. Geochemistry, petrogenesis and geodynamic implications of Paleoproterozoic mafic dykes from the Central Indian Tectonic Zone, central India. Geochem. J. 33, 283–299.
Arita, K., Gautam, P., Ganzawa, Y., 1990. Two metamorphic events of the Nepal Himalayas prior and posterior to India-Eurasia collision. J. Faculty Sci., Hokkaido Uni. 22 (4), 519–528.
Aranovich, L.Y., Lavrent'eva, I.V., Kosyakova, N.A., 1988. Biotite-garnet and biotite-orthopyroxene geothermometers: calibrations accounting for the Al variations in biotite. Geokhimiya 5, 668–676.
Auden, J.B., 1935. Traverses in the Himalaya. Rec. Geol. Surv. India 69, 123–167.
Berman, R.G., 1988. Internally consistent thermodynamic data for minerals in the system Na_2O-K_2O-CaO-MgO-FeO-Fe_2O_3-Al_2O_3-SiO_2-TiO_2-H_2O-CO_2. J. Petrol. 29 (2), 445–522.
Berman, R.G., 1991. Thermobarometry using multi-equilibrium calculations; a new technique, with petrological applications. The Canadian Mineral. 29 (4), 833–855.
Berman, R.G., Aranovich, L.Y., 1996. Optimized standard state and solution properties of minerals. Contrib. Miner. Petrol. 126 (1), 1–24.
Bhargava, O.N., Bassi, U.K., 1994. The Crystalline Thrust Sheets in the Himachal Himalaya and the age of Amphibolite Facies Metamorphism. J. Geol. Soc. India 43, 343–352.
Bhargava, O.N., 2000. Precambrian sequences in the western Himalaya. Geol. Surv. India Spec. Publ. 55, 69–84.
Bhowmik, S.K., Bernhardt, H.-J., Dasgupta, S., 2012. Grenvillian-age assembly of a lower crustal slice beneath the southern granulite terrain of India, with implications for Gondwana reconstructions. J. Geol. 120, 253–275.
Bhowmik, S.K., 2019. The current status of orogenesis in the Central Indian Tectonic Zone: a view from its Southern Margin. Geol. J. 54, 2912–2934.
Bleeker, W., 2003. The late Archean record: a puzzle in ca. 35 pieces. Lithos 71, 99–134.
Brookfield, M.E., 1993. The Himalayan passive margin from Precambrian to cretaceous times. Sed. Geol. 84 (1–4), 1–35.
Brown, M., Johnson, T., Kylander-Clark, A.R.C., 2024. Metamorphic record of the Archean continental crust. In: Roberts, N.M.W., Holder, R.M., Wolfe, M.R., Piccoli, P. M. (Eds.), Earth's Evolving Crust: From the Hadean to the Present. Geol. Soc. London Spec. Publ. 547, 1–30.
Caddick, M.J., Lonopasek, J., Thompson, A.B., 2010. Preservation of garnet growth zoning and the duration of prograde metamorphism. J. Petrol. 51, 2327–2347.
Cawood, P.A., Kroner, A., Pisarevsky, S., 2006. Precambrian plate tectonics: criteriaand evidence. GSA Today 16, 4–11.
Cawood, P.A., Zhao, G.C., Yao, J.L., Wang, W., Xu, Y.J., Wang, Y.J., 2018. Reconstructing south china in phanerozoic and precambrian supercontinents. Ear. Sc. Rev. 186, 173–194.
Cawood, P.A., Wang, W., Zhao, T.Y., Xu, Y.J., Mulder, J.A., Pisarevsky, S.A., Zhang, L.M., Gan, C.S., He, H.Y., Liu, H.C., Qi, L., Wang, Y.J., Yao, J.L., Zhao, G.C., Zhou, M.F., Zi, J.W., 2020. Deconstructing South China and consequences for reconstructing Nuna and Rodinia. Earth Sci. Rev. 204, 103169.
Celerier, J., Harrison, T.M., Webb, A.A.G., Yin, A., 2009. The Kumaun and Garhwal Lesser Himalaya, India. Part 1: structure and stratigraphy. Geol. Soc. Am. Bull. 121, 1262–1280.
Chakrabarty, A., Mukherjee, S., Karmakar, S., Sanyal, S., P.,, 2023. Petrogenesis and in situ U-Pb zircon dates of a suite of granitoid in the northern part of the Central Indian tectonic Zone: Implications for prolonged arc magmatism during the formation of the Columbia supercontinent. Precamb. Res. 387, 106990.
Chattopadhyay, A., Bhowmik, S.K., Roy, A., 2020. Tectonothermal evolution of the Central Indian Tectonic Zone and its implications for Proterozoic supercontinent assembly: the current status. Episodes 43 (1), 132–144.
Condie, K.C., 2002. Breakup of a Paleoproterozoic supercontinent. Gondw. Res. 5 (1), 41–43.
Connolly, J.A.D., 2005. Computation of phase equilibria by linear programming: a tool for geodynamic modelling and its application to subduction zone decarbonation. Earth Planet. Sci. Lett. 236, 524–541.
Corfu, F., Hanchar, J.M., Hoskin, P.W.O., Kinny, P., 2003. Atlas of zircon textures. Rev. Mineral. Geochem. 53, 469–500.
Das, B.P., Joshi, M., Kumar, A., 2019. Tectonochemistry and P-T conditions of Ramgarh and Almora gneisses from Askot Klippe. Kumaun Lesser Himalaya. Acta Geol. Sin. 93 (2), 322–343.
Das, B.P., Joshi, M., Patel, S., Kumar, A., 2021. Tectonometamorphic evolution of the Nappes and Klippes of the NW Lesser Himalaya, India: a review. Indian J. Geosci. 75 (4), 277–295.
Dasgupta, S., Sengupta, P., Guha, D., Fukuoka, M., 1991. A refined garnet-biotite Fe-Mg exchange geothermometers and its application in amphibolites and granulites. Contrib. Miner. Petrol. 109, 130–137.
De Capitani, C., Brown, T.H., 1987. The computation of chemical equilibrium in complex systems containing non-ideal solutions. Geochim. Cosmochim. Acta 51, 2639–2652.
De Capitani, C., Petrakakis, K., 2010. The computation of equilibrium assemblage diagrams with Theriak/Domino software. Am. Mineral. 95, 1006–1016.
DeCelles, P.G., Gehrels, G.E., Quade, J., LaReau, B., Spurlin, M., 2000. Tectonic implications of U–Pb zircon ages of the Himalayan orogenic belts in Nepal. Science 288, 497–499.
Dyck, B., Waters, D.J., St-Onge, M.R., Searle, M.P., 2020. Muscovite dehydration melting: reaction mechanisms, microstructures, and implications for anataxis. J. Metam. Geol. 38, 29–52.
Ernst, R.E., Bleeker, W., Soderlund, U., Kerr, A.C., 2013. Large Igneous Provinces and supercontinents: toward completing the plate tectonic revolution. Lithos 174, 1–14.
Evans, B.W., Guidotti, C.V., 1966. The sillimanite-potash feldspar isograd in western Maine, U.S.A. Contrib. Miner. Petrol. 12, 25–62.
Evans, B.W., 2004. The serpentinite multisystem revisited: chrysotile is metastable. Int. Geol. Rev. 46, 479–508.
Ferry, J.M., Spear, F.S., 1978. Experimental calibration of the partitioning of Fe and Mg between biotite and garnet. Contrib. Miner. Petrol. 66, 113–117.
Gaidies, F., Abart, R., De Capitani, C., Schuster, R., Connolly, J.A.D., Reusser, E., 2006. Characterization of polymetamorphism in the Austroalpine basement east of the Tauern Window using garnet isopleth thermobarometry. J. Metam. Geol. 24, 451–475.
Gansser, A., 1964. Geology of the Himalayas. Interscience Publishers. John Wiley and Sons Ltd., London 289.
Gehrels, G.E., DeCelles, P.G., Ojha, T.P., Upreti, B.N., 2011. Geologic and U–Pb geochronologic evidence for early Paleozoic tectonism in the Dadeldhura thrust sheet, far-west Nepal Himalaya. J. Asian Earth Sci. 42, 1059–1071.
Ghosh, S., Tomson, J.K., Prabhakar, N., Sheth, H., 2023. An extended Neoarchaean to Neoproterozoic history of the Sandmata complex (Aravalli Craton, northwestern India): Insights from metamorphic evolution and zircon-monazite geochronology of high-grade quartzofeldspathic gneisses. Precambr. Res. 394, 107107.
Grenholm, M., Jessell, M., Thebaud, N., 2019. A geodynamic model for the Paleoproterozoic (ca. 2.27–1.96 Ga) Birimian Orogen of the southern West African Craton–Insights into an evolving accretionary-collisional orogenic system. Earth Sci. Rev. 192, 138–193.
Hawkesworth, C.J., Cawood, P.A., Dhuime, B., 2016. Tectonics and crustal evolution. GSA Today 26, 4–11.
Harris, N., Holland, T.J.B., 1984. The significance of cordierite-hypersthene assemblages from the Beitbridge region of the Central Limpopo Belt; evidence for rapid decompression in the Archaean? Am. Mineral. 69, 1036–1049.

Harley, S.L., Kinny, P.D., Snape, I., Black, L.P., 2001. Zircon chemistry and the timing of metamorphism in the Napier complex. Antarctica. J. Petrol. 42, 975–1000.
Harley, S.L., Kelly, N.M., Moller, A., 2007. Zircon behaviour and the thermal histories of mountain chains. Elements 3 (1), 25–30.
Hinsbergen, V.D.J., Lippert, P.C., Dupont-Nivet, G., McQuarrie, N., Doubrovine, P.V., Spakman, W., Torsvik, T.H., 2012. Greater India Basin hypothesis and a two-stage Cenozoic collision between India and Asia. Proc. Natl. Acad. Sci. 109 (20), 7659–7664.
Hifzurrahman, N.P., Yi, K., Anand, A., Misra, S., Champati, A.K., 2021. An ageintegrated geochemical and computational phase-equilibria study from the Wangtu Gneissic complex, N-W Himalaya, and its paleogeographic implications in Columbia assembly. Mineral. Petrol. 115, 365–390.
Hodges, K.V., Silverberg, D.S., 1988. Thermal evolution of the greater Himalaya, Garhwal, India. Tectonics 7 (3), 583–600.
Hodges, K.V., Spear, F.S., 1982. Geothermometry, geobarometry and the Al2SiO5 triple point at Mt. Moosilauke. New Hampshire. Am. Min. 67, 1118–1134.
Hokada, T., Harley, S.L., 2004. Zircon growth in UHT leucosome: constraints from zircon-garnet rare earth elements (REE) relations in Napier complex. East Antarctica. J. Mineral. Petrol. Sci. 99 (4), 180–190.
Holdaway, M.J., Lee, S.M., 1977. Fe-Mg cordierite stability in high-grade pelitic rocks based on experimental, theoretical and natural observations. Contrib. Miner. Petrol. 63, 175–198.
Holdaway, M.J., 2000. Application of new experimental and garnet Margules data to the garnet–biotite geothermometer. Am. Min. 85, 881–892.
Holdaway, M.J., 2001. Recalibration of the GASP geobarometer in light of recent garnet and plagioclase activity models and versions of the garnet–biotite geothermometer. Am. Min. 86, 1117–1129.
Holland, T., Powell, R., 1998. An internally-consistent thermodynamic dataset for phases of petrological interest. J. Metam. Geol. 16, 109–343.
Holland, T., Powell, R., 1991. A compensated Redlich-Kwong (CORK) equation for volumes and fugacities of CO_2 and H_2O in the range 1 bar to 50 kbar and 100–1600 C. Contrib. Miner. Petrol. 109, 265–273.
Holland, T.J.B., Powell, R., 2011. An improved and extended internally-consistent thermodynamic dataset for phases of petrological interest, involving a new equation of state for solids. J. Metam. Geol. 29, 333–383.
Hoskin, P.W.O., Schaltegger, U., 2003. The composition of zircon and igneous and metamorphic petrogenesis. Rev. Mineral. Geochem. 53, 27–62.
Hou, G., Santosh, M., Qian, X., Lister, G.S., Li, J., 2008. Configuration of the late Paleoproterozoic supercontinent Columbia: insights from radiating mafic dyke swarms. Gondw. Res. 14, 395–409.
Imayama, T., Yi, K., Otsuka, M., Uehara, K., Yi, S., 2019. Onset of metamorphism in the Renge metamorphic rocks, Sanbagawa metamorphic belt, SW Japan: evidence from zircon U–Pb ages and petrological studies. J. Metam. Geol. 37, 1075–1095.
Jain, S.C., Yedekar, D.B., Nair, K.K.K., 1991. Central Indian shear zone: a major Precambrian crustal boundary. J. Geol. Soc. India 37, 521–548.
Johansson, A., 2009. Baltica, Amazonia and the SAMBA connection—1000 million years of neighbourhood during the Proterozoic? Precambr. Res. 175 (1–4), 221–234.
Joshi, M., 1984. Sand Mata Paragneiss Complex: Its Structural and Petrologic Analysis (District Udaipur, Rajasthan), unpublished Ph.D. Thesis of Banaras Hindu University, 365p.
Joshi, M., Singh, B.N., 1990. Metamorphism and related deformation around Dhuna Ghat area of Almora Crystallines, Eastern Kumaun Lesser Himalaya, U.P., Proceedings Seminar on Himalayan Geology, Wadia Institute of Himalayan Geology, 6-7 April, 42–43 (Abstract).
Joshi, M., Thomas, H., Sharma, R.S., 1993. Granulite facies metamorphism in Archaean gneiss complex from north-central Rajasthan. Proc. Nat. Acad. Sci. Ind. 63 (A I), 167–187.
Joshi, M., Singh, B.N., Goel, O.P., 1994. Metamorphic conditions of the aureole rocks from Dhunaghat area. Kumaun Lesser Himalaya. Curr. Sci. 67 (3), 185–188.
Joshi, M., 1999. Evolution of the Basal Shear Zone of Almora Nappe. Kumaun Himalaya. Mem. Gondwana Res. Gro. 6, 69–80.
Joshi, M., Tiwari, A.N., 2004. Quartz C- axes and metastable phases in the metamorphic rocks of Almora Nappe. Evidence of Pre-Himalayan Signatures. Curr. Sci. 87, 995–999.
Joshi, M., Tiwari, A.N., 2007. Folded metamorphic reaction isograds in the Almora Nappe, Kumaun Lesser Himalaya: field evidence and tectonic implications. Neues. Fur Geol. Palaont. 244 (2), 215–225.
Joshi, M., Tiwari, A.N., 2009. Structural events and metamorphic consequences in Almora Nappe, during Himalayan collision tectonics. J. Asian Earth Sci. 34 (3), 326–335.
Joshi, M., Das, B.P., Patel, S., 2018. P-T condition of metamorphism in the gneisses of Askot Klippe, Kumaun Himalaya, India. Int. J. Cur. Res. Min. Mat. Metall. Eng. 1, 24–34.
Joshi, M., Kumar, A., Ghosh, P., Das, B.P., Devi, P.M., 2019. North Almora Fault: a crucial missing link in the strike slip tectonics of western Himalaya. J. Asian Earth Sci. 172, 249–263.
Joshi, M., Patel, S., Das, B.P., Oinam, G., Srivastava, T., Kumar, A., 2025. P–T evolution of paleoproterozoic Dangoli Pelitic Gneisses, Baijnath Klippe, NW Himalaya: insights from the geochemistry and Zircon U–Pb geochronology. Isl. Arc 34 (1), e70008.
Kaur, P., Zeh, A., Chaudhri, N., Gerdes, A., Okrusch, M., 2013. Nature of magmatism and sedimentation at a Columbia active margin: Insights from combined U–Pb and Lu–Hf isotope data of detrital zircons from NW India. Gondw. Res. 23 (3), 1040–1052.
Kaur, P., Zeh, A., Chaudhri, N., 2021. Archean to Proterozoic (3535–900 Ma) crustal evolution of the central Aravalli Banded Gneissic complex, NW India: new constraints from zircon U-Pb-Hf isotopes and geochemistry, NW India. Precambrian Res. 359, 106179.
Kirscher, U., Mitchell, R.N., Liu, Y., Nordsvan, A.R., Cox, G.M., Pisarevsky, S.A., Li, Z.X., 2021. Paleomagnetic constraints on the duration of the Australia-Laurentia connection in the core of the Nuna supercontinent. Geology 49 (2), 174–179.
Kohn, M.J., Paul, S.K., Corrie, S.L., 2010. The lower Lesser Himalayan sequence: a Paleoproterozoic arc on the northern margin of the Indian plate. Bulletin 122 (3–4), 323–335.
Kohn, M.J., 2014. Himalayan metamorphism and its tectonic implications. Annu. Rev. Earth Planet. Sci. 42, 381–419.
Kohn, M.J., 2017. The formation of zircon during low-pressure, high-temperature ocean crust alteration. Earth Planet. Sci. Lett. 477, 218–228.
Kusky, T.M., Windley, B.F., Zhai, M.G., 2007. Tectonic evolution of the North China Block: from orogen to craton to orogen. Geol. Soc. Spec. Publ. 280, 1–34.
Kusky, T.M., Santosh, M., Zhu, T., 2016. The transition from divergent to convergent plate boundaries in the North China Craton: implications for the assembly of the Columbia supercontinent. Earth Sci. Rev. 162, 117–133.
Lanari, P., Engi, M., 2017. Local bulk composition effects on metamorphic mineral assemblages. Rev. Mineral. Geochem. 83, 55–102.
Lanari, P., Duesterhoeft, E., 2019. Modeling metamorphic rocks using equilibrium thermodynamics and internally consistent databases: past achievements, problems and perspectives. J. Petrol. 60, 19–56.
Li, Z.X., Zhao, G.C., 2007. Paleoproterozoic collision between the North and South China Cratons: evidence from the Taihang-Wulong suture zone. Precambr. Res. 156, 181–198.
Lihter, I., Larson, K.P., Smit, M.A., Cottle, J.M., Ashley, K.T., Shrestha, S., 2022. Decrypting the polymetamorphic record of the Himalaya. Geology 50 (5), 588–592.
Long, S., McQuarrie, N., Tobgay, T., Rose, C., Gehrels, G., Grujic, D., 2011. Tectonostratigraphy of the Lesser Himalaya of Bhutan: Implications for the along-strike stratigraphic continuity of the northern Indian margin. Bulletin 123 (7-8), 1406–1426.
Lu, S., Li, H., Zhang, C., Niu, G., 2008. Geological and geochronological evidence for the Precambrian evolution of the Tarim Craton and surrounding continental fragments. Precamb. Res. 160 (1), 94–107.
Mandal, S., Robinson, D.M., Kohn, M.J., Khanal, S., Das, O., Bose, S., 2016. Zircon U-Pb ages and Hf isotopes of the Askot Klippe, Kumaun, northwest India: implications for Paleoproterozoic tectonics, basin evolution and associated metallogeny of the northern Indian cratonic margin. Tectonics 35, 965–982.
Martin, E.L., Cawood, P.A., Murphy, J.B., Nance, R.D., Heron, P.J., 2024. The tectonics of introversion and extroversion: redefining interior and exterior oceans in the supercontinent cycle. Geol. Soci. London Spec. Publ. 542, 15–29.
Mazumder, R., Bose, P.K., Sarkar, S., 2000. A commentary on the tectono-sedimentary record of the pre-2.0 Ga continental growth of India vis-a-vis a possible pre-Gondwana Afro-Indian supercontinent. J. African Earth Sci. 30 (2), 201–217.
McQuarrie, N., Robinson, D., Long, S., Tobgay, T., Grujic, D., Gehrels, G., Ducea, M., 2008. Preliminary stratigraphic and structural architecture of Bhutan: implications for the along strike architecture of the Himalayan system. Earth Planet. Sci. Lett. 272, 105–117.
Meert, J.G., 2012. What's in a name? The Columbia (Paleopangaea/Nuna) supercontinent. Gondw. Res. 21 (4), 987–993.
Meert, J.G., 2014. Strange attractors, spiritual interlopers and lonely wanderers: the search for pre-Pangean supercontinents. Geosci. Front. 5 (2), 155–166.
Meert, J.G., Pandit, M.K., 2015. The Archaean and Proterozoic history of Peninsular India: tectonic framework for Precambrian sedimentary basins in India. In: Mazumder, R. & Eriksson, P.G. (Eds), Precambrian Basins of India: Stratigraphic and Tectonic Context. Geol. Soc. Lond. Mem. 43, 29–54.
Meert, J.G., Santosh, M., 2017. The Columbia supercontinent revisited. Gondw. Res. 50, 67–83.
Miller, C., Klotzli, U., Frank, W., Thoni, M., Grasemann, B., 2000. Proterozoic crustal evolution in the NW Himalaya (India) as recorded by circa 1.80 Ga mafic and 1.84 Ga granitic magmatism. Precambr. Res. 103 (3–4), 191–206.
Mishra, D.C., Ravi Kumar, M., 2014. Proterozoic orogenic belts and rifting of Indian cratons: geophysical constraints. Geosc. Front. 5 (1), 25–41.
Mitchell, R.N., Kilian, T.M., Evans, D.A., 2012. Supercontinent cycles and the calculation of absolute Palaeolongitude in deep time. Nature 482 (7384), 208–211.
Molnar, P., Tapponier, P., 1975. Cenozoic tectonics of Asia effects of a continental collision. Science 189 (4201), 419–426.
Margules, M.S., 1895. On the composition of saturated vapors of mixtures. Akademie Der Wissenschaften in Wien, Mathematisch-NaturwissenschaftlicheKlasseAbteilungII 104, 1234–1239.
Moynihan, D., Pattison, D.R.M., 2013. An automated method for the calculation of P-T paths from garnet zoning, with application to metapelitic schist from the Kootenay Arc, British Columbia, Canada. J. Metamorp. Geol. 31, 525–548.
Mukherjee, P.K., Singhal, S., Adlakha, V., Rai, S.K., Dutt, S., Kharya, A., Gupta, A.K., 2017. In situ U-Pb zircon micro-geochronology of MCT zone rocks in the Lesser Himalaya using LA-MC-ICPMS technique. Curr. Sci. 112, 802–810.
Mukherjee, P.K., Jain, A.K., Singhal, S., Singh, N.B., Singh, S., Kumud, S., Seth, P., Patel, R.C., 2019. U-Pb zircon ages and Sm-Nd isotopic characteristics of the Lesser and Great Himalayan sequences, Uttarakhand Himalaya, and their regional tectonic implications. Gondw. Res. 75, 282–297.
Mukherjee, S., Ghosh, G., Sorcar, N., Amal, D.J., Tomson, J.K., Bose, S., 2024. Pre-Himalayan tectono-metamorphic impresses in the Baijnath klippe, Kumaun Himalaya, NW India: implications on a veiled saga of Paleoproterozoic–Neoproterozoic crustal evolution and thermal history of the northern Indian cratonic margin. Geol. Soc. Am. Bull. 137 (1–2), 841–868.
Myrow, P.M., Hughes, N.C., Paulsen, T.S., Williams, I.S., Parcha, S.K., Thompson, K.R., Bowring, S.A., Peng, S.C., Ahluwalia, A.D., 2003. Integrated tectonostratigraphic

analysis of the Himalaya and implications for its tectonic reconstruction. Earth and Plan. Sc. Let. 212, 433–441.
Nance, R.D., Worsley, T.R., Moody, J.B., 1988. The supercontinent cycle. Sci. Am. 259 (1), 72–79.
Nance, R.D., Murphy, J.B., 1994. Orogenic style and the configuration of supercontinents. In: Embry, A.F., Beauchamp, B., Glass, D.J. (Eds.), Pangea: Global Environments and Resources. Can. Pet, Geol, pp. 49–65.
Nance, R.D., Murphy, J.B., 2013. Origins of the supercontinent cycle. Geosci. Front. 4 (4), 439–448.
Nance, R.D., 2022. The supercontinent cycle and Earth's long-term climate. Ann. N. Y. Acad. Sci. 1515 (1), 33–49.
Palin, R.M., Weller, O.M., Waters, D.J., Dyck, B., 2016. Quantifying geological uncertainty in metamorphic phase equilibria modelling; a Monte Carlo assessment and implications for tectonic interpretations. Geosci. Front. 7 (4), 591–607.
Pandey, A., 2022. Geochemical evidence for a widespread Paleoproterozoic continental arc-back-arc magmatism in the Lesser Himalaya during the Columbia supercontinent assembly. Precambr. Res. 375, 106658.
Pant, N.C., Kundu, A., Kumar, R., Dorka, B.S., Prasher, S., 2006. Palaeo-proterozoic metamorphism in the Jeori–Wangtu Gneissic Crystallines (JWGC), western Himalayas. J. Asian Earth Sci. 26, 585–604.
Patel, S., Joshi, M., Oinam, G., Das, B.P., Kumar, A., Srivastava, T., 2025. Magmatic evolution of the Paleoproterozoic A2-type granite along the northern Indian margin: insights from geochemistry and U-Pb geochronology of Baijnath Klippe, NW Himalaya. Geol. Mag. 162 (e5), 1–16.
Pastor-Galan, D., 2022. From supercontinent to superplate: late Paleozoic Pangea's inner deformation suggests it was a short-lived super plate. Earth Sci. Rev. 226, 103918.
Pastor-Galan, D., Nance, R.D., Murphy, J.B., Spencer, C.J., 2019. Supercontinents: myths, mysteries, and milestones. Geol. Soc. Lond Spec. Publ. 470, 39–64.
Patino-Douce, A.E., Harris, N., 1998. Experimental constraints on Himalayan anatexis. J. Petrol. 39, 689–710.
Paton, C., Hellstrom, J., Paul, B., Woodhead, J., Hergt;, J., 2011. Iolite: Freeware for the visualization and processing of mass spectrometric data. J. Anal. At. Spectrom 26 (12), 2508–2518.
Patzelt, A., Li, H., Wang, J., Appel, E., 1996. Palaeomagnetism of cretaceous to Ter-tiary sediments from southern Tibet: evidence for the extent of the northern margin of India prior to the collision with Eurasia. Tectonophysics 259, 259–284.
Paudel, L.P., Arita, K., 2000. Tectonic and polymetamorphic history of the Lesser Himalaya in central Nepal. J. Asian Earth Sci. 18 (5), 561–584.
Perchuk, L.L., Lavrent'eva, I.V., 1983. Experimental investigation of exchange equilibria in the system cordierite-garnet-biotite. In: Saxena, S.K. (Ed.), Kinetics and Equilibrium in Mineral Reactions. Springer-Verlag, New York, pp. 199–239.
Perchuk, L.L., Aranovich, L.Y., Podlesskii, K.K., Lavrant'eva, I.V., Gerasimov, V.Y., Fed'kin, V.V., Kitsul, V.I., Karsakov, L.P., Berdnikov, L.V., 1985. Precambrian granulites of the Aldan shield, eastern Siberia. USSR. J. Metamorphic Geol. 3, 265–310.
Perchuk, A.L., Zakharov, V.S., Gerya, T.S., Griffin, W.L., 2023. Flat subduction in the Early Earth: the key role of discrete eclogitization kinetics. Gondw. Res. 119, 186–203.
Perchuk, A.L., Zakharov, V.S., Gerya, T.S., Stern, R.J., 2025. Shallow vs. deep subduction in Earth history: contrasting regimes of water recycling into the mantle. Precambr. Res. 418, 107690.
Phukon, P., Sen, K., Srivastava, H.B., Singhal, S., Sen, A., 2018. U-Pb geochronology and geochemistry from the Kumaun Himalaya, NW India, reveal Paleoproterozoic arc magmatism related to formation of the Columbia supercontinent. Geol. Soc. Am. Bull. 130 (7–8), 1164–1176.
Phukon, P., 2022. Nature of the northern Indian plate margin during the assembly of supercontinent Columbia: was it a part of a double subduction? Earth-Sci. Revi. 233, 104185.
Pisarevsky, S.A., Biswal, T.K., Wang, X.C., De Waele, B., Ernst, R., Soderlund, U., Cleve, M., 2013. Palaeomagnetic, geochronological and geochemical study of Mesoproterozoic Lakhna Dykes in the Bastar Craton, India: implications for the Mesoproterozoic supercontinent. Lithos 174, 125–143.
Powell, R., Holland, T.J.B., Worley, B., 1998. Calculating phase diagrams involving solid solutions via non-linear equations, with examples using THERMOCALC. J. Met. Geol. 16, 577–588.
Reis, N.J., Teixeira, W., Hamilton, M.A., Bispo-Santos, F., Almeida, M.E., D'Agrella-Filho, M.S., 2013. Avanavero mafic magmatism, a late Paleoproterozoic LIP in the Guiana Shield, Amazonian Craton: U-Pb ID-TIMS baddeleyite, geochemical and paleomagnetic evidence. Lithos 174, 175–195.
Rekha, S., Bhattacharya, A., 2014. Paleoproterozoic/Mesoproterozoic tectonism in the northern fringe of the Western Dharwar Craton (India): its relevance to Gondwanaland and Columbia supercontinent reconstructions. Tectonics 33, 552–580.
Richards, A., Argles, T., Harris, N., Parrish, R., Ahmad, T., Darbyshire, F., Draganits, E., 2005. Himalayan architecture constrained by isotopic tracers from clastic sediments. Earth Planet. Sci. Lett. 236, 773–796.
Rogers, J.J.W., 2000. Origin and fragmentation of the possible approximately 1.5-Ga supercontinent Columbia. Abstracts with programs. Geol. Soci. Am. 32, 455.
Rogers, J.J.W., Santosh, M., 2002. Configuration of Columbia, a Mesoproterozoic supercontinent. Gondw. Res. 5, 5–22.
Rogers, J.J., Santosh, M., 2009. Tectonics and surface effects of the supercontinent Columbia. Gondw. Res. 15 (3–4), 373–380.
Rubatto, D., 2017. Zircon: the metamorphic mineral. Rev. Mineral. Geochem. 83, 261–295.
Saini, N.K., Mukherjee, P.K., Rathi, M.S., Khanna, P.P., Purohit, K.K., 1998. A new geochemical reference sample of granite (DH-G) from Dalhousie, Himachal Himalaya. J. Geol. Soc. India 52, 603–606.
Santosh, M., 2010. Supercontinent tectonics and biogeochemical cycle: a matter of 'life and death'. Geosci. Front. 1, 21–30.
Sawyer, E.W., 1999. Criteria for the recognition of partial melting. Phys. Chem. Earth A Solid Earth Geod. 24, 269–279.
Schaltegger, U., Fanning, C.M., Gunther, D., Maurin, J.C., Schulmann, K., Gebauer, D., 1999. Growth, annealing and recrystallization of zircon and preservation of monazite in high-grade metamorphism: conventional and in-situ U-Pb isotope, cathodoluminescence and microchemical evidence. Contrib. Miner. Petrol. 134, 186–201.
Searle, M.P., 1986. Structural evolution and sequence of thrusting in the High Himalayan, Tibetan—Tethys and Indus suture zones of Zanskar and Ladakh, Western Himalaya. J. Structural Geol. 8 (8), 923–936.
Searle, M.P., 1996. Geological evidence against large-scale pre-Holocene offsets along the Karakoram Fault: implications for the limited extrusion of the Tibetan Plateau. Tectonics 15 (1), 171–186.
Searle, M.P., Szulc, A.G., 2005. Channel flow and ductile extrusion of the high Himalayan slab—the Kangchenjunga–Darjeeling profile, Sikkim Himalaya. J. Asian Earth Sci. 25, 173–185.
Sen, A., Sen, K., Srivastava, H.B., Singhal, S., Phukon, P., 2019. Age and geochemistry of the Paleoproterozoic Bhatwari Gneiss of Garhwal Lesser Himalaya, NW India: implications for the pre-Himalayan magmatic history of the Lesser Himalayan basement rocks. Geol. Soc. Spec. Publ. 481 (1), 319–339.
Sethy, P.C., Maurya, A.K., Singh, P., et al., 2025. Geochemistry and U–Pb Zircon ages of the Bandal Granitoids complex of the Himachal Region, Northwestern Himalaya (India): constraints on crustal evolution and columbia supercontinent assemblage. Geol. J. 1–23.
Sharma, R.S., Sills, J.D., Joshi, M., 1987. Mineralogy and metamorphic history of norite dykes within granulite facies gneisses from Sand Mata, Rajasthan, NW India. Mineral. Mag. 51 (360), 207–215.
Sharma, K.K., Rashid, S.A., 2001. Geochemical evolution of peraluminous Paleoproterozoic Bandal orthogneiss NW, Himalaya, Himachal Pradesh, India: Implications for the ancient crustal growth in the Himalaya. J. Asian Earth Sci. 19 (4), 413–428.
Sinha, R.S., Malhotra, G., Mohanty, M., 1998. Geology of Rajasthan. J. Geol. Soc India, Bangalore.
Sorkhabi, R.B., Stump, E.S., 1993. Rise of Himalaya: a geochronological approach. GSA Today 3 (4), 85–92.
Slama, J., Kosler, J., Condon, D.J., Crowley, J.L., Gerdes, A., Hanchar, J.M., Horstwood, M.S.A., Morris, G.A., Nasdala, L., Norberg, N., Schaltegger, U., Schoene, B., Tubrett, M.N., Whitehouse, M.J., 2008. Plesovice zircon - a new natural reference material for U-Pb and Hf isotopic micro-analysis. Chemical Geo. 249, 1–35.
Smithies, R.H., Champion, D.C., Cassidy, K.F., 2003. Formation of Earth's earlyArchaean continental crust. Precambr. Res. 127, 89–101.
Spear, F.S., Kohn, M.J., Cheney, J.T., 1999. P–T paths of anatectic pelites. Contrib. Miner. Petrol. 134, 17–32.
Spear, F.S., Peacock, S.M., 1989. Metamorphic pressure-temperature-time paths. American Geophy. Uni Washington, p. 102.
Spencer, J.C., Harris, R.A., Dorais, M.J., 2012. The metamorphism and exhumation of the Himalayan metamorphic core, eastern Garhwal region, India. Tectonics 31, TC1007.
Spencer, C.J., Roberts, N.M.W., Santosh, M., 2017. Growth, destruction, and preservation of Earth's continental crust. Earth Sc Rev 172, 87–106.
Srivastava, P., Mitra, G., 1994. Thrust geometries and deep structure of the outer and lesser Himalaya, Kumaun and Garhwal (India): implications for evolution of the Himalayan fold-and-thrust belt. Tectonics 13, 89–109.
Stampfli, G.M., Hochard, C., Verard, C., Wilhem, C., 2013. The formation of Pangea. Tectonophysics 593, 1–19.
Stevens, G., Clemens, J.D., 1993. Fluid-absent melting and the roles of fluids in the lithosphere: a slanted summary? Chem. Geol. 108, 1–17.
Teixeira, J.B.G., Misi, A., Da Silva, M.D.G., 2007. Supercontinent evolution and the Proterozoic metallogeny of South America. Gondw. Res. 11 (3), 346–361.
Terentiev, R.A., Santosh, M., 2020. Baltica (east European Craton) and Atlantica (amazonian and West African Cratons) in the Proterozoic: the pre-Columbia connection. Earth Sci. Rev. 210, 103378.
Tinkham, D.K., Ghent, E.D., 2005. XRMapAnal: a program for analysis of quantitative Xray maps. Am. Min. 90, 737–744.
Thompson, A.B., 1976. Mineral reactions in pelitic rocks; II, Calculation of some PTX (Fe-Mg) phase relations. Am. J. Sci. 276, 425–454.
Thompson, A.B., Algor, J.R., 1977. Model systems for anatexis of pelitic rocks. Contrib. Miner. Petrol. 63, 247–269.
Valdiya, K.S., 1976. Himalayan transverse faults and folds and their parallelism with subsurface structures of north Indian plains. Tectonophysics 32 (3–4), 353–386.
Valdiya, K.S., 1980. Geology of the Kumaun Lesser Himalaya: Dehra Dun, India. Wadia Institute of Himalayan Geology, 291.
Vansutre, S., Hari, K.R., 2010. Granulite belts of Central India with special reference to the Bhopalpatnam Granulite Belt: Significance in crustal evolution and implications for Columbia supercontinent. J. Asian Earth Sci. 39 (6), 794–803.
Vermeesch, P., 2018. Isoplot R: a free and open toolbox for geochronology. Geosci. Front. 9, 1479–1493.
Volante, S., Pourteau, A., Collins, W.J., Blereau, E., Li, Z.X., Smit, M., Gunter, C., 2020. Multiple P–T–d–t paths reveal the evolution of the final Nuna assembly in northeast Australia. J. Metam. Geol. 1–35.
Volante, S., Collins, W.J., Barrote, V., Nordsvan, A.R., Pourteau, A., Li, Z.X., Li, J., Beams, S., 2022. Spatio–temporal evolution of Mesoproterozoic magmatism in NE

Australia: a hybrid tectonic model for final Nuna assembly. Precambr. Res. 372, 106602.
Volante, S., Kirscher, W., 2024. Metamorphic turnover at 2 Ga related to two-stage assembly of Columbia. Nature Sci. Rep. 14, 6483.
Wang, H.Y.C., Chen, H.X., Lu, J.S., Wang, G.D., Peng, T., Zhang, H.C.G., Yan, Q.R., Hou, Q.L., Zhang, Q., Wu, C.M., 2016. Metamorphic evolution and SIMS U-Pb geochronology of the Qingshigou area, Dunhuang block, NW China: tectonic implications of the southernmost Central Asian orogenic belt. Lithosphere 8, 463–479.
Wang, W., Cawood, P.A., Pandit, M.K., Zhou, M.F., Chen, W.T., 2017. Zircon U–Pb age and Hf isotope evidence for an Eoarchaean crustal remnant and episodic crustal reworking in response to supercontinent cycles in NW India. J. Geol. Soc. 174 (4), 759–772.
Wang, W., Cawood, P.A., Pandit, M.K., Xia, X.P., Zhao, J.H., 2018. Coupled Precambrian crustalevolution and supercontinent cycles: Insights from in-situ U-Pb, O- and Hf-isotopes in detrital zircon, NW India. Am. Jour. of Sc. 318 (10), 989–1017.
Wang, W., Cawood, P.A., Pandit, M.K., Zhou, M.F., Zhao, J.H., 2019. Evolving passive- and activemargintectonics of Paleoproterozoic Aravalli Basin, NW India: GSA. Bull. 131 (3–4), 426–443.
Wang, W., Cawood, P.A., Pandit, M.K., 2021. India in the Nuna to Gondwana supercontinent cycles: clues from the north Indian and Marwar Blocks. Am. J. Sci. 321 (1–2), 83–117.
Wang, W., Spencer, C., Pandit, M.K., Wu, Y.-B., Zhao, J.-H., Zheng, J.-P., Xia, X.-P., Lu, G.-M., 2023. Crustal evolution and tectonomagmatic history of the Indian Shield at the periphery of supercontinents. Geochim. Cosmochim. Acta 341, 90–104.
Webb, A.A.G., Yin, A., Harrison, T.M., Célérier, J., Gehrels, G.E., Manning, C.E., Grove, M., 2011. Cenozoic tectonic history of the Himachal Himalaya (northwestern India) and its constraints on the formation mechanism of the Himalayan orogen. Geosph 7 (4), 1013–1061.
White, R.W., Powell, R., Holland, T.J.B., 2001. Calculation of partial melting equilibria in the system Na2O-CaO-K2O-FeO-MgO-Al2O3-SiO2-H2O (NCKFMASH). J. Metam. Geol. 19, 139–153.
White, R.W., Powell, R., Holland, J.B., Johnson, T.E., Green, E.C.R., 2014. New mineral activity-composition relations for thermodynamic calculations in metapelitic systems. J. Metam. Geol. 32, 261–286.
Whitney, D.L., Evans, B.W., 2010. Abbreviations for names of rock-forming minerals. Am. Min. 95 (1), 185–187.
Wilson, J.T., 1963. Evidence from islands on the spreading of ocean floors. Nature 197 (4867), 536–538.
Woodsworth, G.J., 1977. Homogenization of zoned garnets from schists. Canadian Min. 15, 230–242.
Worsley, T.R., Moody, J.B., Nance, R.D., 1985. Proterozoic to recent tectonic tuning of biogeochemical cycles. The carbon cycle and atmospheric CO_2: natural variations Archean to present 32, 561–572.
Wu, C.M., Chen, H.X., 2015. Revised Ti-in-biotite geothermometer for ilmenite or rutile bearing crustal metapelites. Sci. Bull. 60, 116–121.
Wu, C.M., Zhang, J., Ren, L.D., 2004. Empirical garnet-biotite-plagioclase-quartz (GBPQ) geobarometry in medium-to-high-grade metapelites. J. Petrol. 45, 1907–1921.
Wu, C., Wang, G.S., Zhou, Z.G., Zhao, X.Q., Haproff, P.J., 2022. Late Archean–Paleoproterozoic plate tectonics along the northern margin of the North China craton. Geol. Soc. Am. Bul. 135 (3–4), 967–989.
Wu, C., Zhou, Z.G., Zuza, A.V., Wang, G.S., Liu, C.F., Jiang, T., 2018. A 1.9 Ga mélange along the northern margin of the North China craton: Implications for the assembly of Columbia supercontinent. Tect 37 (10), 3610–3646.
Xia, Y., Xu, X., 2019. A fragment of Columbia supercontinent: Insight for Cathaysia block basement from tectono-magmatic evolution and mantle heterogeneity. Geophys. Res. Lett. 46 (4), 2012–2024.
Xiang, H., Zhang, L., Zhou, H., Zhong, Z., Zeng, W., Liu, R., Jin, S., 2008. U–Pb zircon geochronology and Hf isotope study of metamorphosed basic-ultrabasic rocks from metamorphic basement in southwestern Zhejiang: the response of the Cathaysia Block to Indosinian orogenic event. Sci. China (ser. d: Earth Sci.) 51, 788–800.
Yakymchuk, C., Kirkland, C.L., Clark, C., 2018. Th/U ratios in metamorphic zircon. J. Metam. Geol. 36, 715–737.
Yang, P., Shi, M., Tan, F., Rajaure, S., Tripathi, G.N., He, L., Li, Z., Zhan, W., 2021. Zircon U-Pb geochronology and Hf isotopic compositions of Palaeoproterozoic meta-granitoids in the Lesser Himalaya, Nepal: tectonostratigraphic implications. Geol. J. 57 (1), 1–23.
Yardley, B.W.D., Bottrell, S.H., Cliff, R.A., 1991. Evidence for a regional scale fluid loss event during mid-crustal metamorphism. Nat 349, 151–154.
Yedekar, D.B., Jain, S.C., Nair, K.K.K., Dutta, K., 1990. The central Indian collision suture. VisesaPrakasana-BharatiyaBhuvaijñanikaSarveksana 28, 1–43.
Yin, A., Dubey, C.S., Webb, A.A.G., Kelty, T.K., Grove, M., Gehrels, G.E., Burgess, W.P., 2010. Geologic correlation of the Himalayan orogen and Indian craton: Part 1. Structural geology, U-Pb zircon geochronology, and tectonic evolution of the Shillong Plateau and its neighboring regions in NE India. Geol. Soc. Am. Bull. 122 (3–4), 336–359.
Yu, J.H., Wang, L.J., Griffin, W.L., O'Reilly, S.Y., Zhang, M., Li, C.Z., Shu, L.S., 2009. A Paleoproterozoic orogeny recorded in a long-lived cratonic remnant (Wuyishan terrane), eastern Cathaysia Block, China. Precambrian Res. 174, 347–363.
Yu, J.H., O'Reilly, S.Y., Zhou, M.F., Griffin, W.L., Wang, L.J., 2012. U–Pb geochronology and Hf–Nd isotopic geochemistry of the Badu complex, Southeastern China: Implications for the Precambrian crustal evolution and paleogeography of the Cathaysia Block. Precambr. Res. 222–223, 424–449.
Zhang, S., Li, Z.X., Evans, D.A., Wu, H., Li, H., Dong, J., 2012. Pre-Rodinia supercontinent Nuna shaping up: a global synthesis with new Paleomagnetic results from North China. Earth Planet. Sci. Lett. 353, 145–155.
Zhang, J., Li, R., Pandit, M.K., Zheng, J.P., Zhao, J.H., Lan, T.G., Wang, W., 2025. Provenance variation and tectonicevolution of the Vindhyan Basin innorth-central India:Implications onProterozoic supercontinent cycles. Tectonics 44, e2025TC009063.
Zhao, G., Cawood, P.A., Wilde, S.A., Sun, M., 2002. Review of global 2.1–1.8 Ga orogens: implications for a pre-Rodinia supercontinent. Earth Sci. Rev. 59 (1–4), 125–162.
Zhao, G., Sun, M., Wilde, S.A., Li, S., 2004. A Paleo-Mesoproterozoic supercontinent: assembly, growth and breakup. Earth Sci. Rev. 67 (1–2), 91–123.
Zhao, L., Zhai, M., Zhou, X., 2023. Early Precambrian basement components of the Cathaysia Block in South China exhumed by Phanerozoic orogenic events. Precambr. Res. 398, 107218.